TEMPERATURE DEPENDENT OPTICAL PROPERTIES OF SILICON QUANTUM DOT/POLYMER NANOCOMPOSITES

A Thesis
Submitted to the Graduate Faculty
of the
North Dakota State University
of Agriculture and Applied Science

By

Austin Reed Van Sickle

In Partial Fulfillment
for the Degree of
MASTER OF SCIENCE

Major Program:
Materials and Nanotechnology

December 2012

Fargo, North Dakota

ProQuest LLC.
789 East Eisenhower Parkway
P.O. Box 1346
Ann Arbor, MI 48106 - 1346

North Dakota State University

Graduate School

Title

Temperature Dependent Optical Properties of Silicon Quantum Dot/Polymer Nanocomposites

By

Austin Reed Van Sickle

The Supervisory Committee certifies that this *disquisition* complies with North Dakota State University's regulations and meets the accepted standards for the degree of

MASTER OF SCIENCE

SUPERVISORY COMMITTEE:

Erik Hobbie Chair

Andrew Croll

Orven Swenson

Xinnan Wang

Approved by Department Chair:

12/6/12 Date

Erik Hobbie Signature

ABSTRACT

The photoluminescent properties of silicon quantum dots embedded in a stabilizing polymer matrix are relevant to a number of potential applications of these unique nanomaterials such as drug delivery, temperature sensing, and photovoltaics. Aspects of how these photoluminescent properties change with respect to variations in such parameters as excitation intensity, polymer interactions, particle size and particle polydispersity are investigated here. Improving the photostability and understanding the nature of how this is achieved will be critical for realizing the potential of silicon quantum dots in a number of applications. Improvements in photoluminescent stability related to fluorescence intermittency, photoluminescent lifetime, emitted intensity, and wavelength shifts are shown to be due to decreased exposure to oxygen, increased particle packing, decreased temperature, and increased monodispersity of the quantum dots.

ACKNOWLEDGEMENTS

I would like to thank my advisor Dr. Erik Hobbie, with whom my grad school career at NDSU started by meeting on a Thursday, deciding I would start school the next week, on Friday, filling out my grad application Saturday and starting school on Tuesday. The journey continued as we started with one microscope and one LED in the corner of a lab that no one else wanted, buying and building equipment as we went, until we had a respectable lab in our own building two years later. Along the way he allowed me to pursue an extra graduate degree, which I greatly appreciate, that I found I really enjoyed marketing and business, which changed my career path for the better. Thanks for letting me find my own way.

I would also like to thank my partner in SiNCrime, Joe Miller. Our many debates, over many varied subjects, helped to liven up the lab time, while sitting in the dark waiting for data to finish collecting. He would intentionally turn up the air pressure on to our optical table so that whenever it was touched it would make that Darth Vader noise I like so much, and I could always be confident that there were plenty of empty cups, wrappers, and chip bags on the floor of his car, which for some reason annoyed me more than it annoys his wife.

Finally, I would like to thank the rest of our group (John Harris, Matt Semler, Swathi Iyer, Chris Moore, and Loren Vanderhoff) for helping with data collection, physics conversations, and beers at various establishments, the NDSU physics department for allowing me to learn that I like teaching, and Dr. Orven Swenson, Dr. Andrew Croll, and Dr. Xinnan Wang for agreeing to be on my committee and providing support when needed.

TABLE OF CONTENTS

LIST OF FIGURES

CHAPTER 1. INTRODUCTION

Silicon nanocrystals (NCs) or quantum dots (QDs) (in this contribution the term NCs will be used to describe synthesis/production procedures while the term QDs will be used in relation to property characterization) are of great interest in many new fields. Due to their size dependent fluorescent properties, low toxicity [1], good solubility [2], and high mobility [3] they are being used in such applications as biomedical imaging contrast agents [4], photovoltaic devices [5], and optoelectronics. [53] The majority of the recent literature has been and continues to be focused on the properties and applications of NCs synthesized in solutions from precursors of binary alloys such as CdSe, CdS, InAs, and InP. These represent scalable, high yield processes that produce stable monodisperse luminescent colloidal NCs ranging in size from 2 to 10 nm. The synthesis of covalently bonded NCs such as silicon requires a different approach. A recent method uses a scalable single step process in a low-pressure nonthermal plasma. [7] One significant hindrance of this method is the polydispersity of particle sizes as compared to solution growth methods. However, the use of density gradient ultracentrifugation is a scalable method of refining a polydisperse solution of SiNCs into size selected monodisperse solutions. [21] Another property that has prevented extensive use of SiNCs is the rapid oxidation of Si into SiO_2 when exposed to oxygen. Recent theoretical studies point to the significant influence of surface oxidation on silicon quantum dot optical properties. [9] A prevalent hypothesis is that oxygen bonded to the SiNC surface reduces the band gap and limits the emission to the red-orange range of the spectrum. [9][10] The fact that the surface of the SiNCs must be passivated helps to explain why photoluminescence (PL) yield decreases with decreasing particle size, as it is difficult to obtain perfect surface passivation for particles with high curvature. [11] It was demonstrated that by strict avoidance of oxygen during SiNC synthesis and careful surface passivation, relatively high

ensemble PL quantum yields (exceeding 60 %) can be achieved, which puts silicon on a level that can begin to compete with the II-VI direct band gap semiconductors. [7]

One application of particular interest is their use as sensing media in the realm of biomedicine. Other NCs are already in widespread use as a replacement for dyes in biological fluorescent tagging. Silicon NCs are an exciting new nontoxic alternative to the heavy metal NCs currently used in industry. SiNC surfaces can a be easily functionalized with a wide variety of polymers, ligands, etc., which provides an excellent opportunity for sensor development. Temperature, pH, oxygen level, or any number of chemical variables of interest can be measured by appropriately functionalizing the SiNCs and observing the change in optical properties. These functionalized dots can be used as individual fluorescent tags or coated on optical fibers for a more robust, yet small footprint sensor device.

An important property of QDs that has immediate relevance to sensing is the change in photoluminescent properties as a function of temperature. As temperature decreases, there is a significant increase in fluorescent intensity. The change in intensity, the peak wavelength shift, and a change in fluorescent lifetime provide three distinct parameters that might be used to measure temperature. When used in conjunction with optical fiber technology, these changes in photoluminescence with temperature suggest the possibility of producing QD fluorescence based fiber-optic temperature sensors.

Fluorescence intermittency, or “blinking”, of QDs is a process in which individual electrons are excited into a so-called “trap state”. This trap state has a very long lifetime compared to fluorescence, which leads to the reversible process of photobleaching. This causes a decrease in fluorescent intensity as a function of irradiated time, which is a significant problem in sensing accuracy. The extent of photobleaching is extremely sensitive to the surrounding

environment, and increased photostability might thus be induced by the self-assembly of monodisperse QDs into ordered films as well as embedding QDs into a polymer matrix isolating them from environmental factors. [21][23]

An immediate application of Si QD coated fiber optic sensors is in medicine. Cryosurgery at liquid nitrogen temperatures is proving to be an effective way to treat certain internal cancers. However, to completely destroy the tumor it is critical to have a uniform temperature over the target area. [12] Currently employed measures for monitoring and controlling the temperature at the surgery site are based on ultrasound and magnetic resonance imaging, both of which are cumbersome and limited in resolution. The emission from appropriate sized QDs lies in the near infrared (NIR), where biological tissues and fluids are relatively transparent. [13] Using QDs in an application such as this requires that the QDs be protected chemically and mechanically from the surrounding environment. One possible way to do this is through an encapsulation layer of polymer deposited on top of the QD film. The polymer film must adhere to both the fiber and QDs, protect the QDs from stresses imposed by use, chemically stabilize the QDs (namely from oxidation), be stable under intense UV illumination, and be thermally compatible with both the QDs and the optical fiber down to temperatures of 80 K.

This thesis is focused on investigating the photophysical properties of SiQDs that underlie their use in temperature sensing applications. Fluorescence intensity, wavelength, and lifetime are characterized as functions of excitation input power, temperature, particle size and polydispersity, and polymer interactions in the case of polymer/QD nanocomposites. These experiments were also conducted to indirectly observe the influence of ancillary properties such as particle packing, phase separation/mixing, and atmospheric oxygen exposure, on the

photophysics of SiQDs. The conclusion of this contribution presents some brief preliminary work on coating optical fibers with SiQDs, which can be further expanded upon in the future.

CHAPTER 2. PHYSICS OF QUANTUM DOTS

2.1. Quantum Confinement in Silicon

In 1989, it was first realized that the width of the wire-like microstructure of certain forms of porous silicon (pSi) was small enough (< 5 nm) for the optoelectric properties to be strongly affected by quantum confinement (QC). [29] In 1990, efficient, visible, tunable room temperature PL was reported using chemically leached pSi under ultraviolet (UV) excitation. [30] It was proposed that the presence of this PL in the visible was due to QC in the silicon wire, which was also proposed to be crystalline in nature. The hydride passivation of the silicon wires was then proposed to be the reason for the high efficiency of the observed PL. It was later proposed that fluctuations in wire width would have an important effect by localizing excitons and preventing transport to non-radiative centers. [31] These postulates form the basis of the QC model for PL in SiNCs. Examples of UV absorption and PL emission spectra for SiNCs are shown in Figure 1.

Silicon in bulk is an indirect bandgap material, meaning that phonon scattering events are essential to maintain momentum and energy conservation during a radiative event, which further implies that these events will be rare. [14] However, as the size of a Si crystal decreases to the order of ~ 5 nm, symmetry allowed radiative transitions become available due to the periodicity of the Si crystal lattice. [8] This small scale phenomenon, QC, allows for "pseudo-direct" band gap transitions in indirect band gap semiconductors.

Using the effective mass approximation (EMA), based on the Bloch periodic function, the Bohr radius, a, of an electron (e), hole (h), or exciton (X) is given in Equation 1, where $m^*_{e(h)(X)}$ is the effective mass of electron, hole, or exciton, respectively, e is the electric charge,

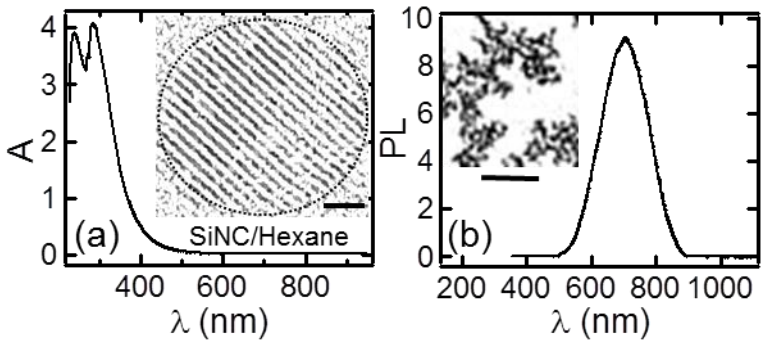

Fig. 1: (a) SiNC/hexane solution UV absorption spectra, Inset: TEM of individual SiNC (scale 1 nm). (b) Emission spectra, Inset: Optical image of typical SiNC film (scale 10 μm).

h is Planks constant, and ε is the dielectric constant. The Bohr radius defines the spatial dimensions of the particle, which determines the range of sizes for which QC can occur. [14] Three confinement regimes can be defined. [32]

$$a_{e(h)(X)} = \frac{\varepsilon\, h^2}{m^*_{e(h)(X)} e^2} \qquad \text{(Eq: 1)}$$

Weak confinement occurs when the dimensions of the system are much larger than both a_e and a_h. The energy is then dominated by the Coulomb term in Equation 2. Medium confinement is defined as occurring when the dimension of the system is much smaller than a_e but larger than a_h; in this case only electrons will experience confinement. This is the regime that most materials belong to. Strong confinement occurs when the dimensions of the system are much smaller than both a_e and a_h. In this case, both the electron and the hole experience confinement, with the Coulomb term being small enough to be treated as a perturbation.

Using the "particle in a box" approach, the ground state energy is taken as the bulk band gap energy, E_g. To solve for the variation of band gap energies with nano-structure size the

general field Hamiltonian for a system of Coulombic interacting particles, given in Equation 2, can be employed. [33]

$$\mathcal{H} = \int d^3r\psi^\dagger(r)\left(\frac{-\hbar^2}{2m}\nabla^2\right)\psi(r) + \frac{1}{2}\int d^3r d^3r'\psi^\dagger(r)\psi^\dagger(r')\frac{e^2}{4\pi\varepsilon|r-r'|}\psi(r)\psi(r') \quad \text{(Eq: 2)}$$

Here, ψ is the field operator, m is the mass of the electron or hole, ε is the dielectric constant of the surrounding medium and e is the electric charge. The field operators can then be expanded in a two-band model for the conduction band, C, and the valence band, V, shown in Equation 3, where k represents a summation over momentum states.

$$\psi(r) = \sum_k a_{k,i}\varphi_{k,i}(r)(i \in C, V) \quad \text{(Eq: 3)}$$

The $\varphi_{(k,i)}$ e basis set is expanded to reflect an infinite confinement potential with a Bloch basis. The infinite potential used is a reasonable assumption for a NC embedded in a matrix (i.e. SiO_2) with a higher E_g than the NC. While Bloch states reflect the periodic nature of the crystal, the boundary conditions for a NC do not reflect this same periodicity. However, in this solution the interesting transitions are assumed to occur near the Brillouin zone center, and while this may not be strictly accurate, $\mathbf{k} \cdot \mathbf{p}$ perturbation theory considers expansions about the Brillouin zone minimum, $\mathbf{k_0}$. Therefore using Bloch states through the use of the slowly varying wave approximation, where only the $\mathbf{k_0} = 0$ states are used, is acceptable. Equation 1 is then solved in the exciton basis using the state Φ, Equation 4, defined as an e-h pair above the ground state, Φ_0.

$$\Phi = \sum_{k1,k2} C_{k1,k2} a_{k1}^\dagger b_{k2}^\dagger \Phi_V \quad \text{(Eq: 4)}$$

$$\Phi_V = b_{k3} b_{k4} \ldots b_{kN} \Phi_0 \quad \text{(Eq: 5)}$$

Here a_k (b_k) refers to electrons (holes) in the conduction (valence) band. Now expanding in low lying k-states near the band edge, equation 6 is solved giving the band gap energy variation. [14]

$$E_g(D) = <\Phi|\mathcal{H}|\Phi> \quad \text{(Eq: 6)}$$

The effective mass calculated from the density of states, which is related to the parabolic structure of the band gap, is used for the mass terms in Equation 1. [34] This calculation results in the equation relating the band gap energy to the size of the NC, Equation 7.

$$E_{gap}(D) = E_{gap}(\infty) + \frac{A}{D^2} \quad \text{(Eq: 7)}$$

Here, $E_{gap}(\infty)$ is the band gap of the bulk material, A is a scaling parameter which is different for each confinement regime, while D is the NC diameter. [14] The important result of this calculation is the inverse relationship between the band gap energy and the NC diameter. There have been numerous attempts using various methodologies and approximations to accurately simulate and fit experimental data regarding the band energy shift in NCs [14][33-36]. While exact numbers for both the parameter A, and the exponent of D (2 in this solution) may differ among various NC synthesis methods and simulation algorithms, there is one key result. As the NC size decreases, the band gap increases. PL arises due to QC allowed radiative transitions across this wider bandgap. Because of the inherent in-direct nature of the band gap in SiNCs, "pseudo-direct" transitions are allowed at small sizes, (or likely always in the inner core of larger NCs) and indirect transitions tend to dominate as the NC size approaches the QC limit of ~ 8 nm. [11] These phonon assisted transitions lead to longer excited state lifetimes and wider PL linewidths, or thermal broadening. Narrowing this linewidth is essential for SiNCs to compete with direct band gap NCs such as CdSe. A comparison of linewidth for polydisperse SiNCs, monodisperse SiNCs, and monodisperse CdSe NCs is shown in Figure 2.

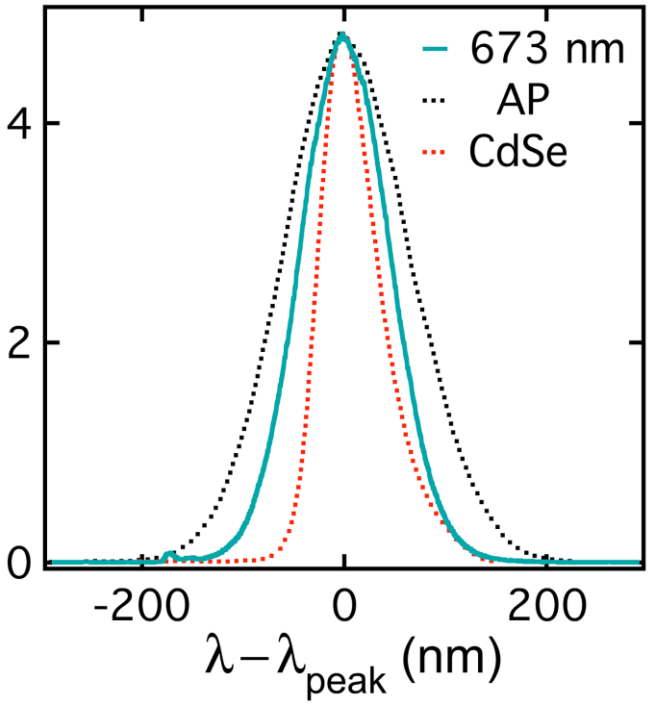

Fig. 2: Spectral linewidth of commercially available CdSeNCs, Polydisperse SiNCs (AP), Monodisperse SiNCs (673 nm). [21]

2.2. Oxidation and Surface Passivation

Silicon is a material that undergoes rapid oxidation when exposed to air. The resulting oxide coating can have significant effects on PL in NCs. The effect of oxygen has been investigated by several groups [10][37][38] with widely varying conclusions.

In one experiment, the oxide passivation effects were studied as a function of time. The size distributions were determined *in situ* with a time-of-flight mass spectrometer (TOFMS). Figure 3(a) shows the evolution of the PL spectra of a size-selected sample when it was exposed to air for different periods of time. The average diameter of the SiNCs was determined by TOFMS to be $d \sim 3.6$ nm while the full width at half maximum (FWHM) of the size distribution was $\Delta d = 0.6$ nm. Before exposure to air, no PL could be detected. After 20 mins, a peak arises at around 1.72 eV, and within one day, the peak shifts to 1.85 eV. At later times, the effect is much smaller and seems to be saturated. Thus, after 25 days, the PL peak has experienced only a

small further shift to 1.87 eV. As the maximum of the PL band shifts to higher energies, its width also increases. Over the same period, the FWHM varies from 0.23 eV for the first spectrum to 0.31 eV after 25 days. The evolution of these two parameters (position and width of the PL band) as a function of time is summarized in Figure 3(b). It has also been shown by high-resolution transmission electron microscopy that aged SiNCs are surrounded by an oxide shell with a thickness of approximately 10% of the total particle diameter. It was found that, for a given particle size, the spacing of the {111} lattice plane fringes varies by ~2%. This variation, which can be explained by different degrees of oxidation and thus different stresses exerted on the crystalline lattice, results in an inhomogeneous "oxide-induced" PL bandwidth of 0.25 eV for a given particle size in an aged sample. [38]

Similar results indicating a blueshift of PL spectra over time have been reported by several groups [21][37]. As the SiNC shell oxidizes, surface Si atoms bond with oxygen, thus reducing the size of the optically active core, which increases the emission energy as predicted in QC. While this effect can degrade desirable properties over time, it has been demonstrated [7][37] that quantum yield and PL intensity can be increased through careful oxidation of NCs. This improvement is believed to be a result of terminating dangling surface bonds, which removes localized states inside the band gap but does not modify the intrinsic nature of the highest occupied molecular orbital (HOMO) and the lowest unoccupied molecular orbital (LUMO). [9]

A contradictory result was discovered, however, where the opposite effect predicated by QC was observed under oxidation. [10] PSi samples that initially exhibited PL from blue to orange actually redshifted, with the PL intensities decreasing under oxidation. The magnitude of the redshift increased with increasing porosity (decreasing particle size). The gradual passivation of the NC surface from $Si - H_n$ (n = 1-3) bonds to Si – O – Si and Si – O – H

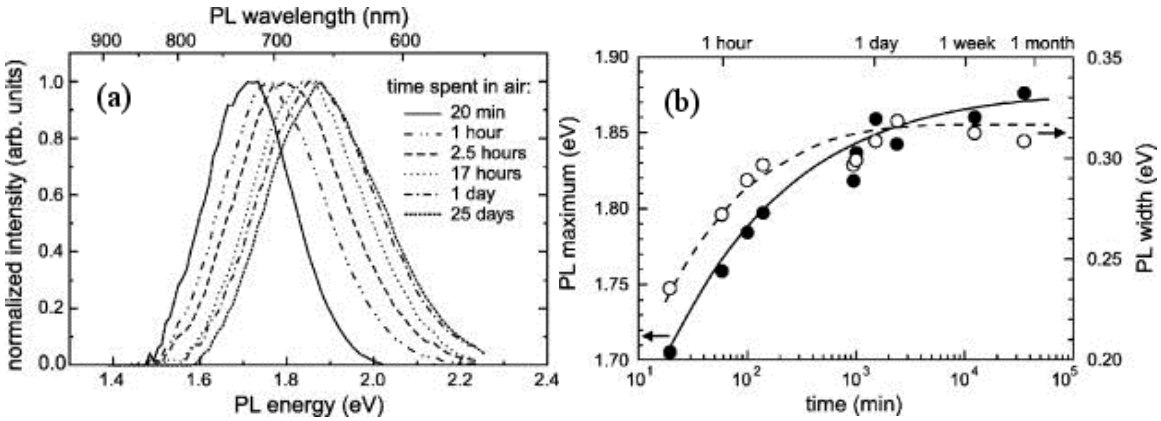

Fig. 3: (a) Evolution of the amplitude-normalized PL spectra for a size-selected sample exposed to air for different cumulative time, (b) *Evolution of the peak position (filled symbols, solid curve, and left-hand side y-axis) and FWHM (open circles, dashed curve, and right-hand side y-axis) of the PL band as a function of the time the sample was exposed to air. Data and figure are reproduced from Ref. [38].*

redshifted the PL until FTIR spectroscopy indicates stabilization occurs. It was then argued that both NC size and surface chemistry dictate the recombination mechanism. In instances where there exists a Si/SiO_2 interface, some of the Si – O – Si bonds may weaken or break due to the large interfacial stress, in which case Si = O covalent bonds can form, stabilizing the surface. This covalent bond induces a localized stable electronic state or even a trapped exciton. For larger NCs (> 3 nm), QC effects dominate and surface passivation does not cause a redshift as the band-gap is too small to stabilize the Si = O bond. For intermediate (3 > NC > 1.5 nm) sizes, recombination involves a trapped electron and a free hole leading to a smaller correlation between size and PL energy. For small NCs (< 1.5 nm) oxygen has a direct chemical interaction with the Si orbitals that substantially changes the HOMO and LUMO as compared with H passivation. Calculations explain the experimental results that 1- to-2 nm H-passivated NCs tend to emit in the blue/violet for dipole-allowed transitions whereas core/shell oxide-passivated NCs tend to emit in the yellow-red for dipole-forbidden transitions. Both types of NCs can have high luminescence quantum yields because the competing rates of nonradiative multiphonon

relaxation are very low in the absence of structural defects. For these sizes, the excited state is a surface excitation directly involving the capping atoms rather than a volume excitation. Recombination is thus via trapped excitons. [9][10] The overall effect of oxidation is widening of the band gap.

Since numerous studies have indicated the adverse effects of oxidation on PL properties, active passivation of NCs has become common practice. A process known as hydrosilylation [39] is widely used. This reaction, which is thermally activated, causes alkenes or alkynes to bond with hydrogen passivated silicon surfaces. This then allows grafting of organic molecules like octadecene to the surface. This treatment, while allowing slight further oxidation [7], effectively prevents large-scale oxidation, creates stable colloidal particles soluble in organic solvents, and allows further surface functionalization.

It is important to note that while both NC size and surface chemistry affect the PL properties, they indirectly imply that surface effects can be considerable. As NCs get smaller, the percentage of optically active atoms in the NC that reside on the surface of the crystal increases. The NCs then move into the strong confinement regime, where both the electron and hole wave function extend outside the physical dimensions of the NC. As noted earlier, this causes different recombination mechanisms than in the larger, QC constant, NCs. Also, due to the high surface curvature, complete passivation gets increasingly less likely for smaller sizes. This effect may be seen in the decrease of QY with decreasing NC size. [7][21]

2.3. Fluorescence Intermittency

Fluorescence intermittency, also known as blinking, refers to the switching of a quantum emitter between a bright (on) state, and a dark (off) state. It is a common phenomenon that seems to follow the same rules in all quantum emitters, ranging from single dye molecules to

semiconductor NCs. While this process can be useful in some instances, i.e. single emitter identification, [40] it causes problems such as reduced quantum yield and reduced brightness, in many other applications.

The statistics of both on and off times have been widely investigated in direct band gap QDs, i.e. CdSe, [41][42] with the conclusion that QD's on/off times follow a power law relationship, Equation 8, where $P(\tau)$ is the probability that a QD will be in on/off state

$$P(\tau) \propto \tau^{-\beta} \qquad \text{(Eq: 8)}$$

at a given time, and β is the power law exponent, found experimentally to be between 0.5 and 2. [27][41][43][45] Experimental data do not always fit precisely to this model, but corrections [44] have been proposed that allow for a more accurate description. While there were questions whether the indirect nature of the bandgap in Si would result in different statistics, it has been shown that Si does indeed follow a power law correlation. [40][43] An example of SiQD blinking measured by our group is shown in Figure 4, which clearly shows the binary nature of the blinking process.

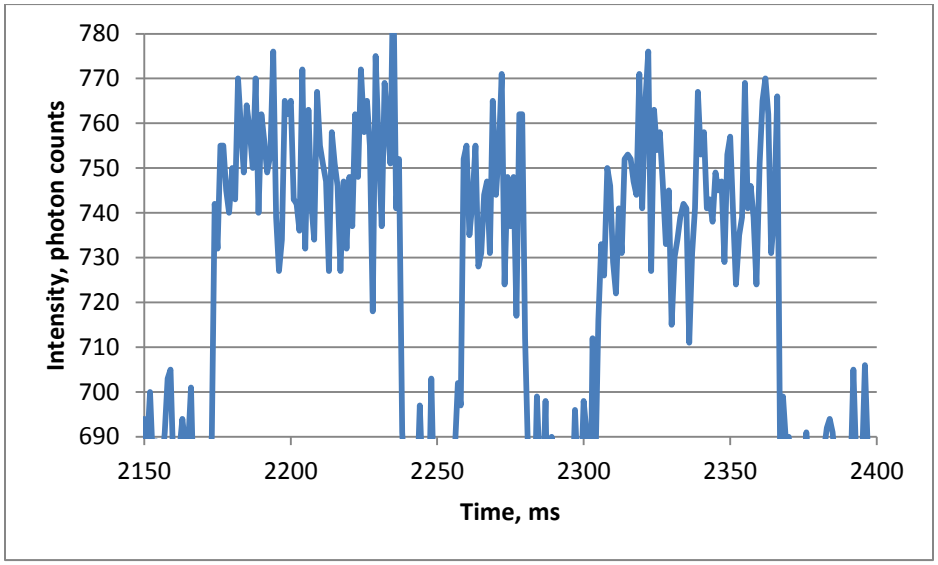

Fig. 4: SiQDs blinking over 2.5s, where the peaks are "on" times and the valleys "off" times.

While there is still debate in the literature over the exact mechanisms of blinking, it is widely accepted that charge carriers become delocalized from the QD core and become "trapped" in long-lived surface or external trap states. The nature of these trapped states is not fully understood, however lattice imperfections, shell imperfections, and external environmental factors are all thought to contribute. The subsequent ionization of the core renders the QD non-emitting for long periods of time due to Auger recombination. [46] Auger recombination occurs when a core hole is filled by a higher-level electron. The energy released is then coupled into another electron, ejecting it from the QD. The QD can eventually switch "on" by neutralization of the core through de-trapping of the ionizing charge or migration of the core charge to the surface. [27][44] Ionization suppression is thus a desirable area of study. Figure 5 provides an illustration of two ionized particles in proximity. The two wavefunctions are drawn so as to indicate the overlap of edge localized charge distributions. Through this mechanism, it is suggested that electronic repulsion might be used through particle packing to suppress ionization. Indeed, it has been shown that hexagonal packed monodisperse QD films do appear to exhibit improved PL properties when compared to polydisperse films. [21]

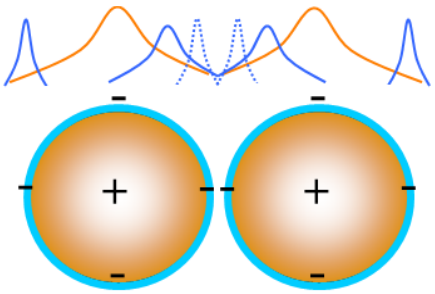

Fig. 5: Ionized NCs and subsequent overlap in electron-hole wavefunction.

This phenomenon of blinking gives rise to a property termed bleaching, where the intensity of PL observed from a QD ensemble decreases over time to a steady-state equilibrium. This fully reversible property is caused by a buildup of excitons in long-lived non-emitting

trapped states. Methods for minimizing or eliminating this effect are explored later in this thesis. An example spectra, Figure 6, illustrating bleaching collected from a QD rich film created by using a polydisperse (AP) solution of roughly 5 % by mass in hexane. PS spheres of 10 μm diameter were deposited on the four corners of a thin glass cover slip as spacers and a droplet of QD/hexane solution was deposited in the center. A second cover slip was then placed on top and the sample was set inside a sealed glass chamber filled with hexane vapor for 24 hours.

2.4. Fluorescent Lifetime

Electron-hole fluorescent recombination lifetime is the time it takes for an excited electron to recombine with the vacant hole. In direct bandgap QDs, this recombination lifetime is on the order of nanoseconds. However, indirect semiconductors exhibit two distinct exponential lifetimes. The short lifetime, ~10-100 ns, derives from the "pseudo-direct" transitions allowed through QC, while the much longer lifetimes, ~10-1000 μs, arise from indirect transitions due to the necessity of the momentum conserving phonon. PL lifetime or emission decay from a pulsed laser input is fit using a stretched exponential decay, Equation 9.

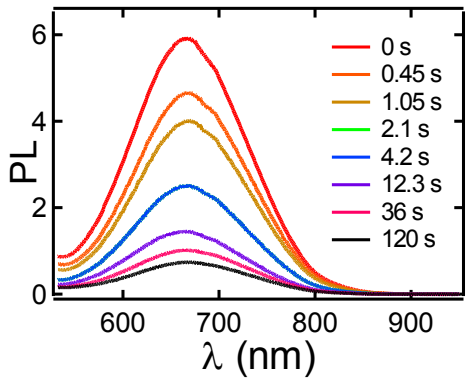

Fig. 6: Bleaching spectra from a SiQD film collected over 2 minutes.

$$I(t) = I_0\, e^{(-t/\tau)^{\alpha}} \qquad \text{(Eq: 9)}$$

Here, the intensity at given time, *I(t),* is related to the initial intensity, I_0, the fluorescent lifetime, τ, and the stretching exponent, α. The stretching exponent, $\alpha \sim 0.7$ for SiQDs at room temperature, likely arises from the multiple relaxation pathways that are allowed with the indirect band gap. [21] This lifetime also exhibits the proportionality shown in Equation 10, where τ is the lifetime, E is the emitted photon energy and E^* = 0.2 eV. [47][48]

$$\tau \propto e^{(-E/E^*)} \qquad \text{(Eq: 10)}$$

Measurements of the PL lifetime give insight into the efficiency of energy transfer between the excited and ground states by providing a temporal value related to the excited state decay time.

CHAPTER 3. PREPARTION OF MONODISPERSE SILICON NANOCRYSTALS

3.1. Plasma Synthesis of Silicon Nanocrystals

Over the twenty year history of SiNCs, there have been many different methods developed to synthesize these materials, including laser pyrolysis of silane gas [11], electron beam lithography and reactive or plasma etching [6][13], and the widely used method of ion implantation in SiO_2 films. [14][15] Here we use SiNCs synthesized through a more recent method involving non-thermal plasmas. [16][17]

A schematic and photo of the non-thermal plasma synthesis reactor is shown in Figure 7. A mixture of argon, silane in argon and hydrogen is introduced from the top of the reaction tube. Radio frequency power at a level of 20-50 W at 10-30 MHz [16][17] is applied to the electrode pair, which leads to a breakdown of the gas and the generation of an electron plasma. The plasma electrons reach temperatures of 20,000 – 50,000 K or approximately 2 – 5 eV, while the gaseous atoms and ions remain near room temperature. [16] The energetic plasma electrons dissociate the silane precursor and chemical clustering leads to the formation of silicon clusters. The gas and particles exist in the plasma zone for 2-5 ms, during which the particles grow to 2 – 6 nm. The particles are then collected on a stainless steel mesh. The particles are produced in a vacuum environment in which they are protected from oxygen and water, which minimizes particle oxidation. The particles are transferred to a nitrogen atmosphere where they are passivated using organic molecules, in this case either 1-dodecene or 1-octadecene, through hydrosilylation. The use of fourier transformed infrared spectroscopy (FTIR) gives strong evidence that the C = C bonds in the organic molecules break to form Si – C bonds with surface silicon atoms, however the overall surface coverage is unclear. [17] The SiNCs are then

transferred into organic solvent solutions such as hexane, toluene, chloroform, or m-xylene for storage and experimentation.

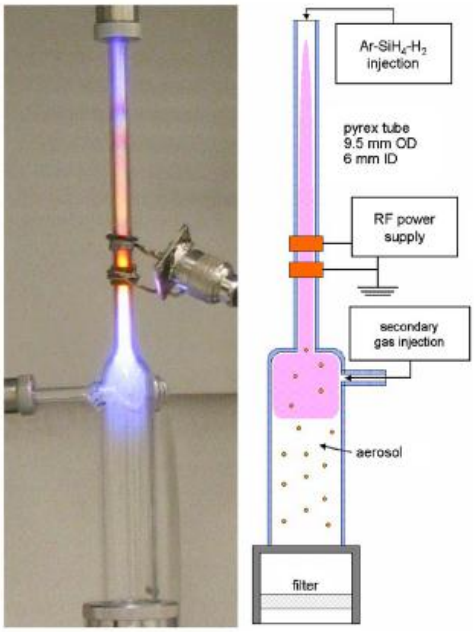

Fig. 7: Schematic of non-thermal plasma reactor. Figure is reproduced from Ref. [17].

3.1.1. Quantum Yield

An important measure of the quality of SiNCs is the quantum yield (QY), η, which can be defined for either an individual or ensembles of SiNCs as expressed in Equation 11.

$$\eta = \#\ of\ emitted\ photons\ /\ \#\ of\ absorbed\ photons \qquad \text{(Eq: 11)}$$

Initial QYs reported were under 10%, which is believed to be due to the rapid oxidation of the SiNCs, which in turn degrades luminescent properties. [9] Passivation with organic molecules raised that number to 23% [18] and 30% [19]. It was further demonstrated that by strict avoidance of oxygen during synthesis and careful surface passivation, the QYs could be raised to 60% [7][16][17], which is on par with direct band gap semiconducting NCs. Quantum yield can be measured by introducing a UV/blue LED into an integrating sphere by way of an optical fiber. The radiation filling the sphere is then analyzed using a fiber-coupled spectrometer. An initial

baseline spectra is taken by introducing a vial with the solvent used in the colloidal NC solution which shows the excitation peak of the LED. Next, a vial of the NC solution is introduced, which shows a strongly reduced excitation peak due to the absorption by the NCs, and a broad peak at the PL emission wavelength. Subtracting the baseline from the sample spectrum, the spectrum showing both the absorption and emission peaks is obtained. This spectrum can then be used to calculate QY. [17]

3.2. Size Separation Using Density Gradient-Ultracentrifugation

SiNCs produced through the above mentioned non-thermal plasma process produces a mean size of 3 – 4 nm, $<R>$, and a standard deviation of ~1.3 nm, σ. This gives a polydispersity index (*PDI*), Equation 12, range of 1.05 – 1.11, which is excellent for as-produced (AP) SiNCs. [21]

$$PDI = 1 + \frac{\sigma^2}{<R>^2} \qquad \text{(Eq: 12)}$$

However, entropic crystallization cannot occur unless the standard deviation in particle size is 12% of the mean, which corresponds to a critical PDI of 1.02. [22] This crystallization allows close particle packing, which in turn, seems to enhance the QY and decrease bleaching or promote brightening in a NC ensemble. [21] Thus, NC crystallization might be a desirable outcome for certain applications.

A scalable method for size separation of SiNCs that has been used effectively for separating carbon nanotubes [64] is density gradient ultracentrifugation (DGU). This method exploits the relation of particle size and density with buoyancy and viscous drag in a high gravity environment.

Organic solvents of chloroform and m-xylene are used to create a five-step solvent density gradient. They are combined into 50%, 60%, 70%, 80%, 90% chloroform by volume in

m-xylene. The step gradient is layered by first micropipetting 1.4 mL of the 90 % solution into the bottom of a custom-made polyvinylidene fluoride ultracentrifuge tube. Each successive layer of decreasing density solution is carefully micropipetted on top of the last. A 0.3 mL solution of AP SiNCs in m-xylene (1mg/mL) is then deposited on top of the gradient. The gradient solution is then centrifuged at 30,000 rpm at 1°C for 10 hours. Glass tipped micropipettes are used to collect 200 µL fractions starting at the top. Typically, approximately 30 fractions are collected per centrifuge run. Fractions 1-7 contain the smallest NCs (D < 2 nm) and impurities; these fractions are generally undesirable for data collection. Fractions 8-18 typically contain monodisperse solutions of NCs with peak spectral wavelength differences of 5 – 10 nm between fractions, ranging in size from 3 – 5 nm. Fractions greater than 19 contain larger particles and aggregates which are indistinguishable spectrally from the parent material. [21] Typical spectra are shown in Figure 8. [23] The actual fraction numbers that fall into these three categories vary from batch to batch, however comparing spectral data between batches allows the combination of fractions from different batches as a way to increase the available experimental material.

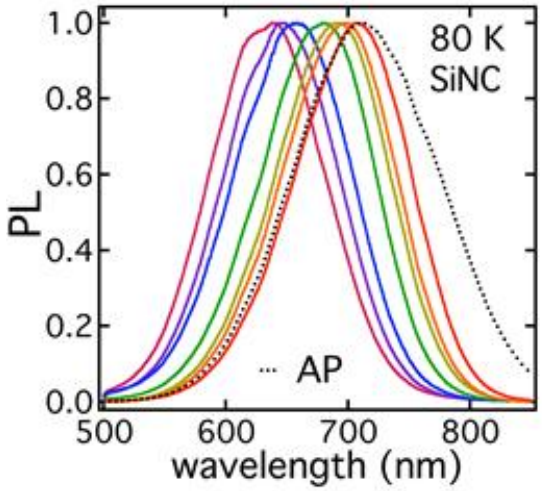

Fig. 8: Monodisperse SiNC fraction spectra at 80K, parent material (AP). [23]

CHAPTER 4. POLYMER/QUANTUM DOT NANOCOMPOSITES

4.1. Polymer/QD Nanocomposites

The ability to efficiently disperse and assemble NCs in polymer structures and films has profound implications for a variety of established processes, as well as new experimental applications. While there has been much work on the use of polymer/NC nanocomposites in photovoltaic, [24][25] and optical devices, [26][74] less attention has been focused on biocompatible nanocomposite applications. These bio-composites require both polymer and NCs with acceptable cytotoxicity levels, for use in such areas as biomedical sensing and drug delivery. [75] Thus, the issue of the kinetics of NC assembly from solution, and the subsequent morphology influence on desirable physical properties, i.e. PL must be explored in these biocompatible nanomaterials. This chapter explores PL properties comparing pure QD films to polymer/QD films and various polymer/QD nanocomposite schemes.

4.2. PL Emission Wavelength and Intensity Shifts with Excitation Power

The PL properties of QDs are greatly affected by a variety of external factors. In this section the excitation power applied to a thick film of pure AP QDs and a thick film of polystyrene (PS) doped with AP QDs was varied from 0.04 mW to 1 mW. The results are then compared to determine the influence of the PS matrix on the QD PL properties.

4.2.1. Procedure

The QD sample was prepared with the method outlined in section 2.3. A second sample was prepared using PS with a molecular weight of 200,000 and a radius of gyration of 20 nm. A solution of 3 % QDs and 5 % polymer in toluene was prepared. A circular film of approximately 1 mm in diameter on a glass substrate was produced by spin coating, which is shown in Figure 13 (c-d). The subsequent morphology of the QD/PS nanocomposite film was characterized by a

ridge of PS around the circumference of the film. Using a 5x objective, it can easily be seen that under UV excitation there is bright PL in the thick polymer ridge, indicating an effective inclusion of QDs in the PS matrix.

Visible-NIR fluorescence spectroscopy for this experiment was performed using a customized epi-illumination inverted microscope with a gray scale CCD (Adimec1000) camera for visualization and a scientific grade spectrometer (Ocean Optics QE6500) calibrated for a wavelength range of 350-1500 nm. Excitation was provided by a fiber-coupled 365 nm, variable power 1mW LED, which was collimated to a minimum illumination area of 100 μm through a 60x water-immersion, 1.20 NA objective, which translates to 2 W/cm^2 at the sample. Power measurements were done by placing a UV enhanced silicon photodetector (Newport 818-UV, 200 nm – 1100 nm) connected to a bench top optical power meter (Newport 1928-C) over the objective and recording the maximum power obtained. The power measurement calibration was done by measuring the output when input is maximum. The maximum output of the LED was measured to be 1 mW, I_{in}, while the value measured at the objective was 0.186 mW, I_{out}.. Scaling the output power using I_{out} / $I_{in,}$ relative power was used to characterize the results.

The power of the LED was varied to observe relative output powers of: 1, 0.9, 0.8, 0.7, 0.6, 0.5, 0.4, 0.3, 0.2, 0.1, 0.08, 0.06, and 0.04. Spectra were collected on two spots on each of the QD and QD/PS samples, starting with relative power 1 and ending with 0.04, with one power per day using a 50 ms integration time for 120 s.

4.2.2. Results and Discussion

The data in Figure 9 show that the initial emission intensity increases linearly with increasing relative power while the wavelength blueshifts with increasing power. It can also be seen that the QD and QD/PS wavelengths follow a similar curve.

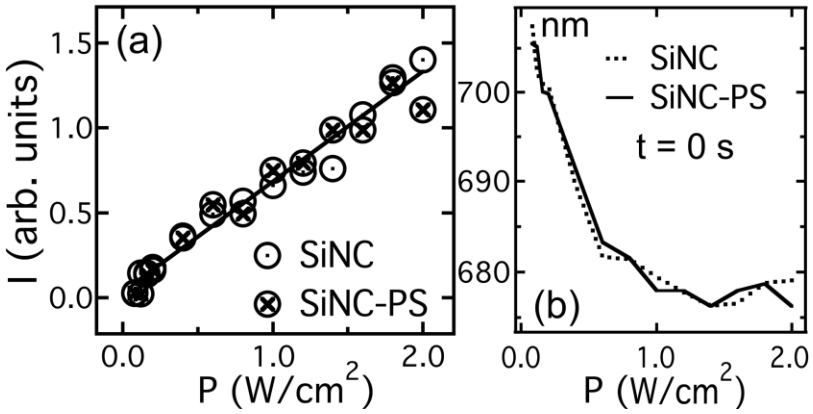

Fig. 9: (a) Initial intensity vs. power. (b) Initial wavelength vs. power.

Normalized intensity *I(t)/I(0)*, provides a convenient measure of photostability. As shown in Figure 10(a-b), the bleaching exhibits power law decay at late times [27] with an exponent of ¼. PL half-life is considered here to be a simple measure of PL stability, and it can be seen that the QD/PS film displays improved stability over the QD film. By measuring half-life in the QD/PS film, Figure 10(c), it was observed that there is a power-law correlation between initial intensity and half-life, which shows an exponent of 1.5, while finally in Figure 10(d) the PL half-life dramatically decreases with increasing power. This figure also indicates an improvement in PL stability for the QD/PS film.

4.3. Comparison of PL Temperature Dependence of APQD and PS/APQD Films

Photobleaching and the associated wavelength shift, along with PL lifetime as a function of temperature, were studied by comparing a pure QD sample to a QD/PS sample.

4.3.1. Procedure

Visible-NIR fluorescence spectroscopy for this experiment was performed using a customized upright microscope with a gray scale CCD (Adimec1000) camera for visualization and a scientific grade spectrometer (Ocean Optics QE6500) calibrated for a wavelength range of 350-1500 nm. Excitation was provided by a fiber coupled 365 nm, variable power 1mW LED,

collimated to a 10x UV (325 nm – 500 nm), 0.25 NA high-power focusing objective with a 15 mm working distance (by way of a UV enhanced aluminum coated mirror) through a high transmission 50 nm bandpass filter centered at 377 nm, into a 4x objective for transmission fluorescence. The custom optical setup is shown in Figure 11. All subsequent experiments use this setup unless otherwise noted.

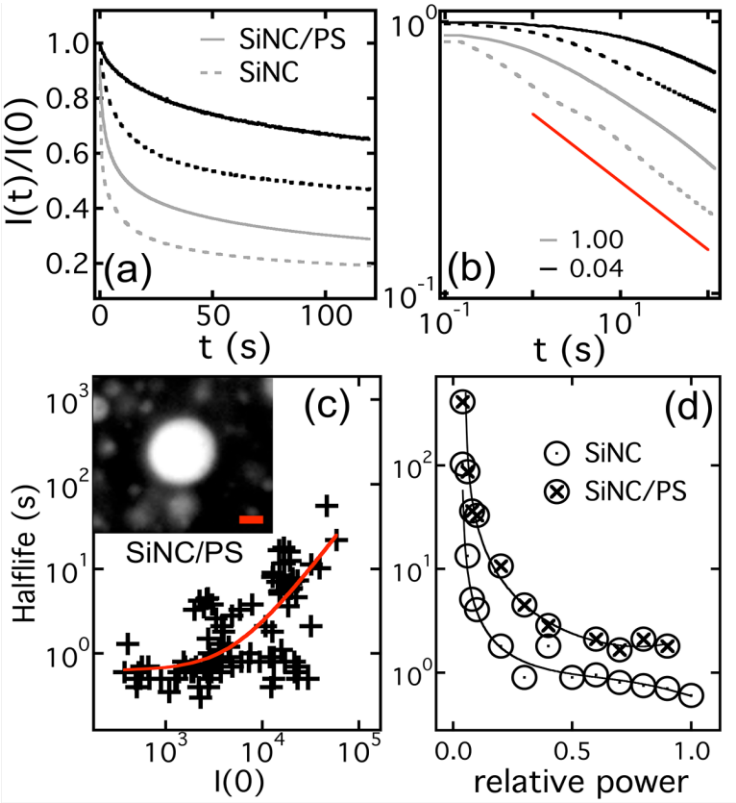

Fig. 10: (a) Normalized intensity vs. time. (b) Intensity vs. time for high intensity (1.00) and low intensity (.04), red line indicates a power law exponent of .25. (c) Half-life vs. initial intensity, power law fit indicates an exponent of 1.5. (d) Initial intensity vs. relative input power.

Particle packing has been shown to increase photostability, [21] suggesting that films should be prepared as densely as possible. One method to achieve this is by enhancing the hydrophobicity of the glass slides used for sample preparation. This increases the contact angle between a solvent drop and the glass, minimizing the contact area. As the solvent evaporates,

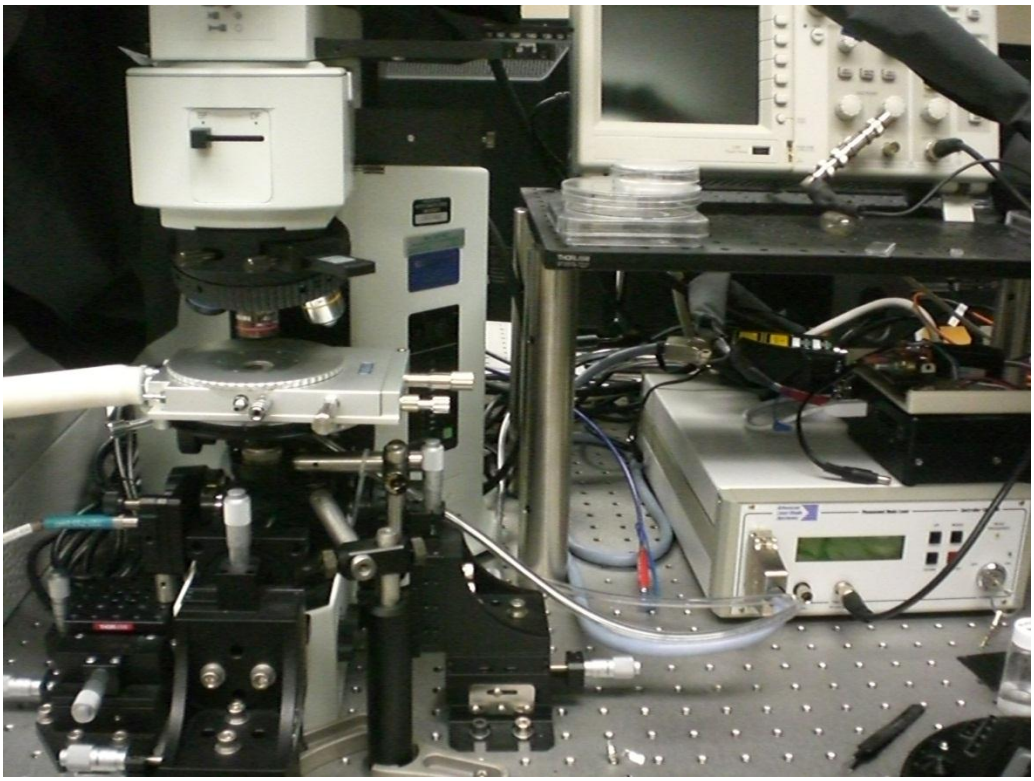

Fig. 11: Custom upright microscope setup.

the colloidal particles aggregate closer to the center of the droplet, producing densely populated areas. This hydrophobicity can be enhanced by first UVO plasma cleaning the slides and then annealing them in perfluorodecyltriethoxsilane vapor to generate a fluorinated self-assembled monolayer (SAM). [21] Capillary forces in a pipette immersed into a solution will induce a small volume of liquid to be confined in the tip when removed from the liquid, which can be released by covering the other end of the pipette. Using this method, very small drops can be repeatedly deposited on the SAM treated slides, creating a small material rich sample. This method can also be used as an approximate volume measurement for sample preparation, i.e. drops of the same solvent deposited from a pipette will have approximately equal volumes. This method of sample production and volume measurement is used in all subsequent experiments unless otherwise noted.

The QD sample was prepared using an AP polydisperse solution of roughly 5% QD in hexane. Twenty droplets of solution were deposited onto a SAM treated glass substrate and allowed to dry in atmosphere. The QD film is shown in Figure 12(a-b). The PS/QD film was described in the previous section.

These samples were then studied over the course of 24 days. Cooling was done using a cryostage (Linkam BSC196) capable of achieving temperatures down to 77 K (liquid nitrogen). Each sample was cooled down on subsequent days from 300 K to 80 K. After the sample was cooled and had reached thermal equilibrium (~15 minutes at temperature), spectral data and lifetime were then collected at each temperature.

Lifetime was obtained by using a 375 nm, 140 mW, 20 ps pulsed laser (Advanced Laser Systems PiLas) with a repetition rate of 1 kHz as an excitation source (1 kHz was chosen to allow five separate lifetimes to be acquired). Photon detection was done using a photomultiplier tube (PMT) (Hamamatsu H10721-20) with a custom-built power supply, shown in Figure 13, input into an oscilloscope (Tektronix TDS 1012B) analyzed with Labview's Tektronix Signal Analyzer package. The signal was time averaged at 1 waveform/sec for at least 2500 seconds, depending on the initial intensity. The subsequent waveform, which contains five averaged lifetimes, is combined to create one lifetime with at least 12,500 averages. This curve is then fitted using a stretched exponential function to obtain the lifetime.

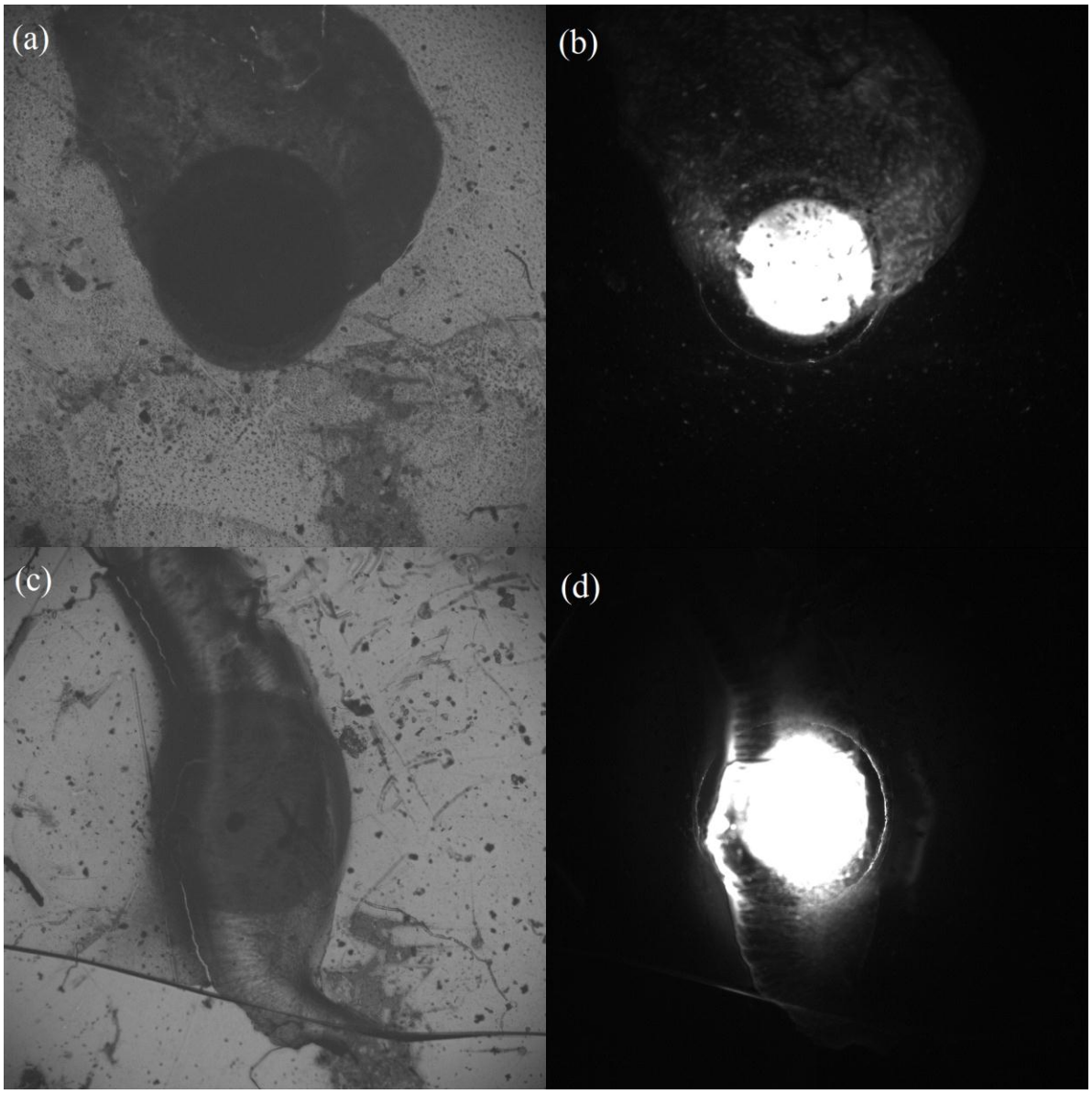

Fig. 12: (a) Bright field image under 4x magnification of SiQD film where the dark circle is the aperture of the cryostage. (b) Dark field PL image of SiQD film. (c) Bright field image of SiQD/PS film. (d) Dark field PL image of SiQD/PS film.

4.3.2. Results and Discussion

Figure 14(a, d) shows the collected spectra over the 80-300 K range of the QD film and the QD/PS film, respectively. The solid lines (a, d) indicate the spectra at time zero, while the dashed line corresponds to time 2 minutes, thus illustrating the photobleaching effect. Figures 14(b, e) are the normalized intensity versus temperature. The start and end designations indicate

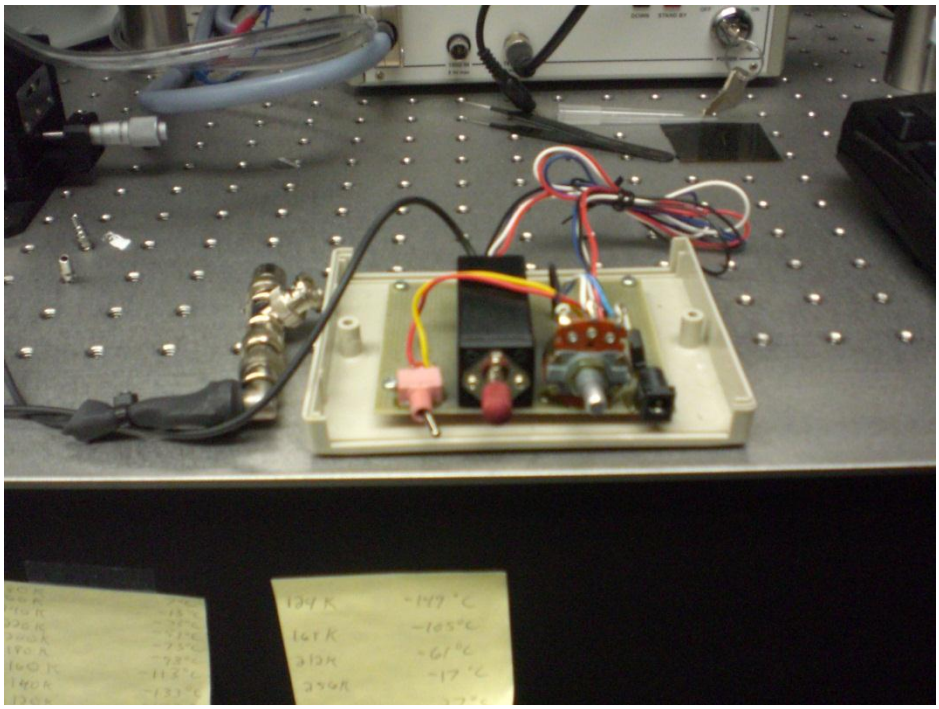

Fig. 13: PMT with custom built power supply.

photobleaching over the two minute collection time. From this data it can be seen that there is greater temperature dependence in the QD/PS films as compared to the pure QD, as the PL intensity increases by a factor of ~2.5 from 300 K to 80 K. This indicates an enhancement of sensitivity to temperature, which is desirable in a sensing probe. Figures 14(c, f) display the wavelength as a function of temperature. It should be noted the drop in each at roughly 225 K, which characterizes an increase in photobleaching, is an indication that the nitrogen atmosphere inside the cryostage is being permeated by atmospheric oxygen. The stage cools by pumping liquid nitrogen through a sample holding platform, which then vents the boiled nitrogen gas back into the stage to eliminate water condensation on the view windows. However, as the temperature increases past 200 K, the pump speed decreases, allowing oxygen to enter back into the environment. This is further evidence of the necessity for isolating the QDs from oxygen.

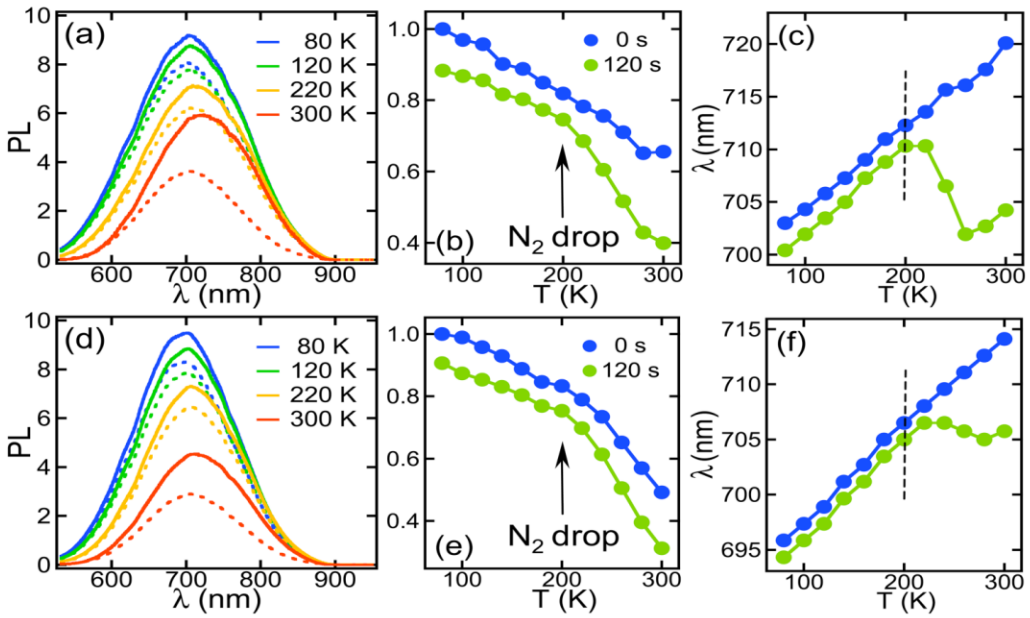

Fig. 14: (a) PL decay as a function of temperature for a QD cluster. (b) Corresponding PL peak intensity as a function of temperature, and (c) wavelength of peak emission as a function of temperature. (d) PL decay as a function of temperature for a QD/PS cluster. (e) Corresponding PL peak intensity as a function of temperature, and (f) wavelength of peak emission as a function of temperature.

The lifetimes are shown in Figure 15(a-c). It can be seen that both QD and PS/QD lifetimes increase as the temperature decreases. However, the polymer does not seem to have a significant effect on the lifetime value.

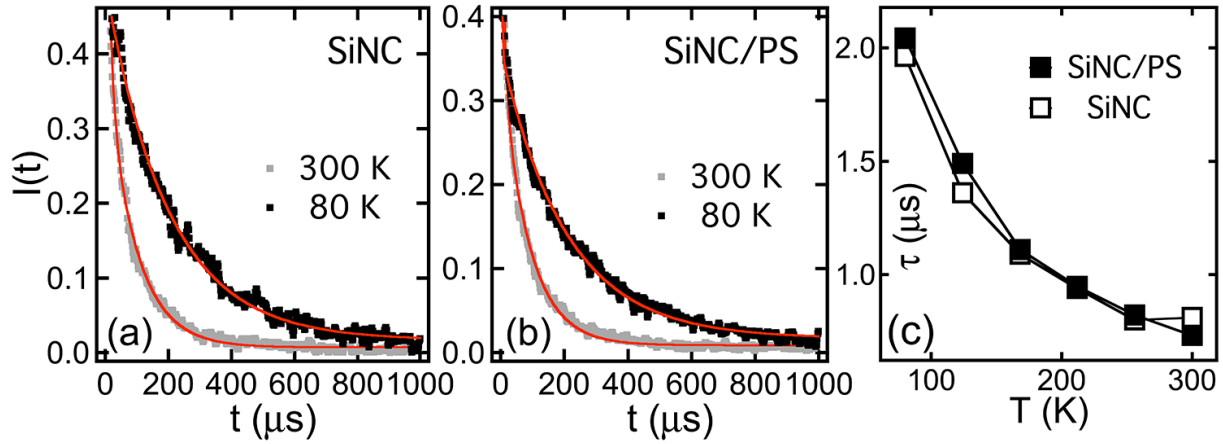

Fig. 15: (a-b) Radiative lifetime curves at 80 and 300 K for SiNC and PS/SiNC nanocomposite. (c) Comparison of the lifetimes.

4.4. PL Properties of Nanocomposites Using Varied Molecular Weights of PS and PMMA

In this section, the influence of polymer molecular weight on PL is investigated. PS and polymethylmethacrylate (PMMA) were used as polymers in the nanocomposites studied.

4.4.1. Procedure

Solutions of 3 % by weight PS and PMMA in toluene were prepared for a variety of molecular weights (MW). Mixtures of QD/polymer/toluene were then produced using a 1:1 drop ratio of APQD solution to polymer solution. PS MWs used were 700,000, 200,000, 100,000, 12,000, and 8,000, while PMMA MWs were 100,000, and 40,000. Polymer/QD films of each polymer and weight were produced using the procedure outlined in 4.3.1.

4.4.2. Results and Discussion

The morphology of the nanocomposite films varied with different polymer molecular weight. It can be seen in Figure 16(a-b) that as the MW increases there is a smaller QD/PS rich ridge around the circumference of the drop. This is a clear example of the well-known "coffee ring" effect. The capillary forces induced during the evaporation of solvent will cause an edge-directed flow that transports particles to the contact line in an irreversible fashion. [28] This indicates that the larger MW QD/PS composite particles get transported to the edge of the drop more slowly due to increased viscosity. Indeed, in observing evaporation, polymer included films stayed the same size as the original droplet, indicating pinning of the polymer to the glass around the edge of the drop. PL distribution is highest in the thick outer ridge, indicating effective phase mixing.

The PMMA/QD films, Figure 16(c-d), displayed a similar thick edge, however it was not nearly as prevalent. Under visual inspection rings can be seen radiating inward from the edge in contrast to the uniform appearance of PS/QD. The PL distribution was much more even

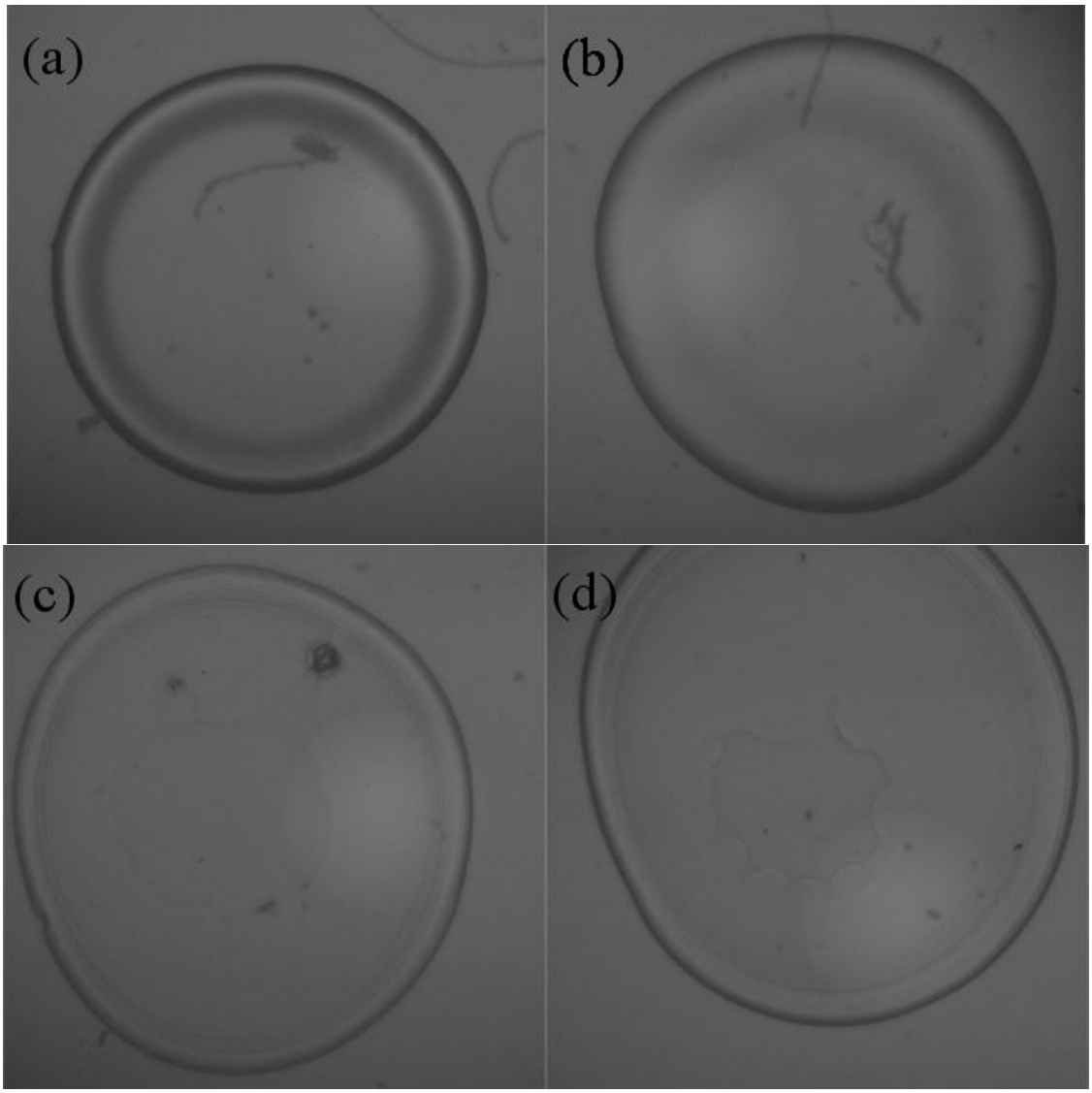

Fig. 16: (a) 100,000 MW PS/QD. (b) 8,000 MW PS/QD. (c) 100,000 MW PMMA/QD (d) 40,000 MW PMMA/QD.

throughout the film, which could be a byproduct of the more uniform PMMA film. PL data observing both bleaching and wavelength shift indicate some overall trends but are somewhat inconsistent. PMMA and low MW 12,000 PS seem to improve photostability over the larger PS, however the 8,000 MW PS appears in line with the larger molecules. All of the polymers do show an improvement over the APQD, indicating once again that the addition of a polymer matrix enhances PL stability for APQDs. The PMMA also indicates a much smaller, almost negligible, wavelength shift compared to PS or APQD. The temperature dependence of these

properties was investigated, however, it was discovered that PMMA possesses a phase transition at ~200 K associated with absorbance of H_2O molecules into the polymer matrix. This phase transition significantly affected the PL intensity, causing a drop in emitted intensity at 200 K. This effectively eliminates PMMA as a possible polymer in SiQD/polymer temperature dependent nanocomposite applications.

CHAPTER 5. POLYDIMETHYLSILOXANE SILICON QUANTUM DOT NANOCOMPOSITES FROM MONODISPERSE FRACTIONS

5.1. PL Temperature Dependence of Monodisperse QD Fractions and PDMS/MQDF Films

The PL properties of SiQDs have been intensively studied, but due to the difficulty in producing batches of monodisperse QDs, there is little data in the literature on such purified materials. Using density gradient ultracentrifugation (DGU), monodisperse QD solutions in the size range of 4.7 nm to 3.2 nm with a polydispersity index of 1.01 to 1.02 [21] can be easily produced. Through QC, these size-selected fractions are predicted to emit higher energy PL with shorter radiative lifetimes as the size decreases. [21]

Also of interest are the temperature dependent photoluminescent properties of QDs, which have potential relevance to thermal sensing media for applications such as cryosurgery at liquid nitrogen temperatures. It has been reported for CdSe QDs that the radiative lifetime significantly increases as the temperature decreases [49-51], while the PL intensity increases five-fold [49], with the largest effect below 50 K. Although of interest for purely scientific reasons, this regime of very low temperature is not of interest for medical applications.

SiQDs have also been shown to exhibit similar radiative lifetime and PL intensity increases at low temperature. [15] These properties, coupled with low cytotoxicity, make SiQDs an attractive alternative to the heavy metal QDs that have been most heavily studied. A biocompatible polymer matrix is essential for this type of application. Polydimethylsiloxane (PDMS) is widely accepted as a biocompatible polymer and is currently being used in a variety of healthcare applications from vocal cord treatments to biocompatible coatings for microfluidic devices. [65][66]. Nanocomposites of PDMS and monodisperse SiQDs are studied in this section.

5.2. Procedure

Size-selected (monodisperse) SiQD fractions were prepared in organic solutions using the procedure described Chapter 3. Three batches of fractions were used; one for QD fractions (QDF) and two for PDMS/QDF.

The QDF solutions initially in m-xylene/chloroform solvent mixture were transferred into toluene by vacuum evaporation. Once the solvent evaporated, nitrogen gas was used to release the vacuum, minimizing oxygen exposure and thus oxidation. Two drops of toluene, using the measurement procedure in 4.3.1, were used as solvent for the new solution. Samples were then prepared on SAM treated glass slides by using the droplet drying technique described in 4.3.1 to produce dense QDF films. All of the QDs available in each fraction solution were used for each sample.

Each fraction, from 8-16, was prepared as a film and then measured immediately. Cooling was done on the setup described in 4.3.1. The sample was initially cooled to 80 K at a cooling rate of 10 K/min and was allowed to sit for 10 minutes to attain thermal equilibrium. Spectral data were then collected for 20 s with an integration time of 50 ms, The procedure described in section 4.3.1 was used to measure radiative lifetime. Spectra and lifetimes were measured at 80 K, 124 K, 168 K, 212 K, 256 K, and 300 K in that order for each fraction.

PDMS prepared at monomer (Sylgard 184 elastomer base)/crosslinker (Sylgard 184 elastomer curing agent) ratios of 10:1, 5:1, and 1:1 were initially tested in nanocomposites with AP QDs to ascertain the most desirable ratio for use. Visual PL observation indicated better phase mixing occurs with a larger monomer/crosslinker ratio, however PL properties were not measurably different. 10:1 ratio was selected due to a familiarity with this mixture within our research group. A 10:1 by weight of monomer to crosslinker PDMS mixture was combined in a

vial and stirred for 5 minutes. A small amount (< 100 mg) of the mixed PDMS was placed in another vial and then combined with toluene to form a 2 % by weight PDMS/toluene solution. This parent solution was then used for the subsequent preparation of all PDMS/QDF samples.

In order to ensure sufficient PL intensity to collect meaningful lifetime data, two batches of comparable QDFs were combined. Each fraction's spectrum was initially collected using a 365 nm LED as excitation. Fractions from each batch whose peak wavelengths were within 5 nm were combined by adding several extra drops of toluene to each solution, ensuring maximum colloidal solubility (QDs adhere to the glass vials over time, rendering a large portion of the QDs unusable) and then depositing all of one fraction into the other, drop by drop. These solutions were then concentrated by vacuum evaporation (1 to 2 drops of solvent left is ideal). Once concentrated, each combined fraction had 1 drop of PDMS solution added. Additional solution concentration was performed as needed. As with pure fractions, one PDMS/QDF sample was made and measured per day to minimize oxidation.

Each sample was produced on a SAM glass slide by the drop procedure described in 4.3.1. Once all of the solvent from the vial was exhausted, the sample was placed in a vacuum, 25 mm Hg, and baked at ~40^{o}C for at least 1 hour to ensure PDMS crosslinking. Once baking was complete spectra and radiative lifetime were collected as described for pure QDF.

5.3. Results and Discussion

The PL spectra at 80 K for both the parent QD film and the fractions were shown earlier, in Figure 9. It should be noted that the linewidths are among the lowest reported for SiQDs but are still around 1.4x that of commercially available CdSe at comparable emission wavelength, which was shown in Figure 2. All samples exhibited a shift to lower emission energy with increasing temperature attributed to thermally induced changes to the QC energy levels. [23]

These energy shifts are a complex function of lattice expansion, wave-function distortion, mechanical strain, and electron-phonon coupling. [67] While bulk silicon is dominated by the combined effects of thermal expansion and electron-phonon coupling, [68][69] QDs thermal expansion contributes to the QC energy levels as a function of temperature, E(T), through a dependence of the bandgap on lattice spacing. [67] This contribution, while small in the QC regime, is also proportional to the thermal expansion coefficient of Si which changes sign near 100 K, but is otherwise small (~ 10^{-6} K^{-1}) . [70] Expansion of the QC volume is similarly small, while the surrounding matrix of PDMS or pure QDs ensure that any thermal expansion mismatch creates minimal strain. [67] Electron-phonon coupling is thus the dominant contribution to the QC energy level shifts. Since an expression for the temperature dependent QC energies of nanocrystallite silicon does not exist, we fit the data to a second order polynomial in temperature (Figure 17(a)), where the constant term is the 0 K band gap. Using the bulk band gap at 0 K, setting A = 4.53, and adjusting the exponent to 1.5 [21] gives Equation 13, used to fit the band gap

$$E_{gap}(D) = 1.17 + \frac{4.53}{D^{1.5}} \qquad \text{(Eq: 13)}$$

energies for both pure QDF and PDMS/QDF in Figure 17(b). The emission energies are shown in Figure 17(a) as a function of temperature. [23] The linewidth was found to be similar for both sample types for the largest fractions while the PDMS nanocomposites exhibited narrower linewidths for the smaller QD size, which can be seen in Figure 18. [23] All samples displayed a full width at half maximum (FWHM) that increases with decreasing temperature, consistent with reported results for QDs embedded in SiO_2 at comparable emission energies. [71]

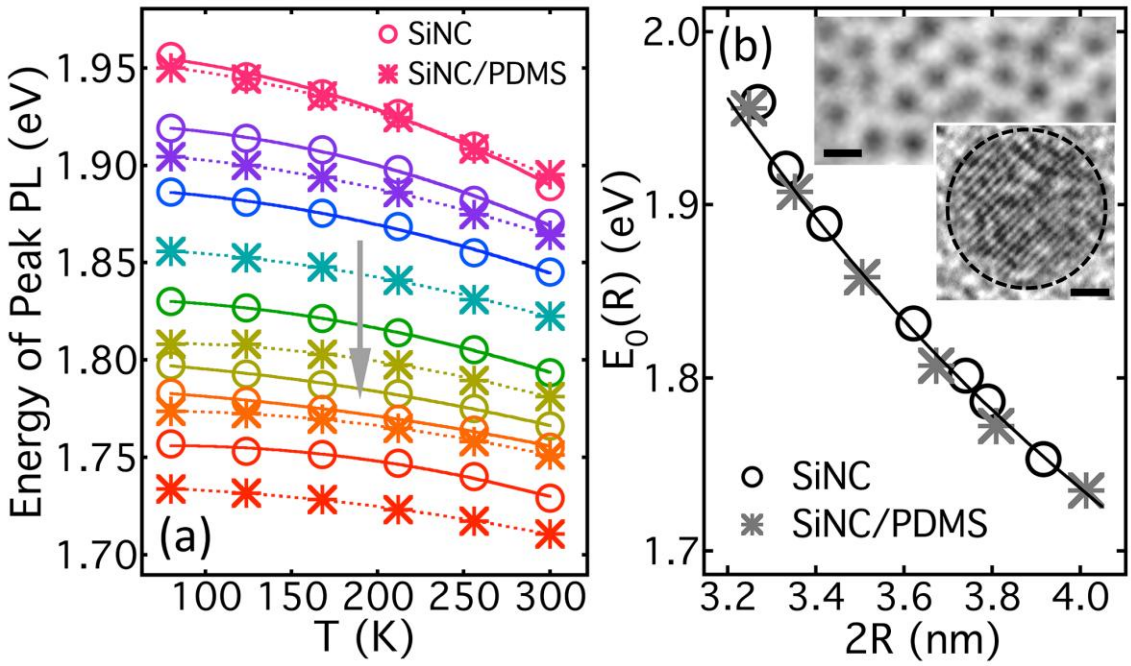

Fig. 17: (a) Temperature dependence of the energy of peak PL for both pure SiNC fractions and PDMS nanocomposites, where the arrow indicates the direction of increasing size. (b) Size dependence of the 0 K bandgap, where the upper insets show TEM images of a typical fraction (top, 5 nm scale) and a single nanocrystal (bottom, 1 nm scale). [23]

These differences in linewidth are accompanied by a shift in PL lifetime. The PL decay exhibits a stretched exponential decay, Equation 9, as discussed in section 2.4, which is likely caused by the indirect bandgap nature of Si. The stretched nature of the relaxation leads to noticeable curvature on a semi-log plot, as shown in in Figure 19(a,b) which shows the stretched exponential lifetime curves at three temperatures. It can easily be seen that the lifetime increases dramatically with decreasing temperature. Figure 19(c,d) shows lifetime maps of the samples in the plane of temperature and QD size. Comparing the two film types indicates similar trends, with an increase in lifetime with both increasing QD size and a decrease in temperature. [23]

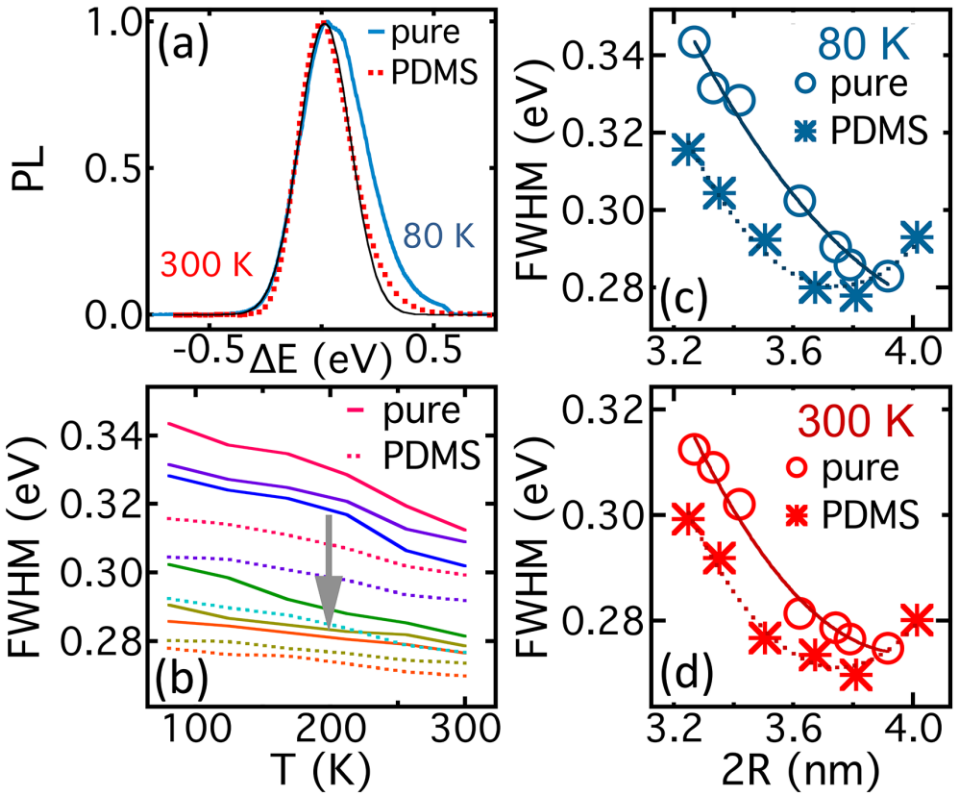

Fig. 18: (a) Typical spectra. (b) PL linewidth (FWHM) as a function of temperature for the pure QD fractions and the corresponding PDMS nanocomposites, the arrow indicates the direction of increasing nanocrystal size. (c) FWHM for the QD fractions and nanocomposites as a function of nanocrystal size at 80 K and (d) an analogous plot at 300 K. The curves are second order polynomial fits. The horizontal label in (c) is identical to that in (d). [23]

The evolution of the stretching exponent, α, with temperature is shown in Figure 20(a). The trends of both QDF and PDMS/QDF films indicate an increase in α upon cooling. Figure 20(b) shows lifetime versus temperature, while Figure 20(c) shows the change in lifetime with respect to QD size at 80 and 300 K. It can be seen that while the trends for both film types exhibit similar characteristics, the pure QDF lifetimes increase with decreasing size at low temperatures, which is in contrast to the PDMS nanocomposite results. [23]

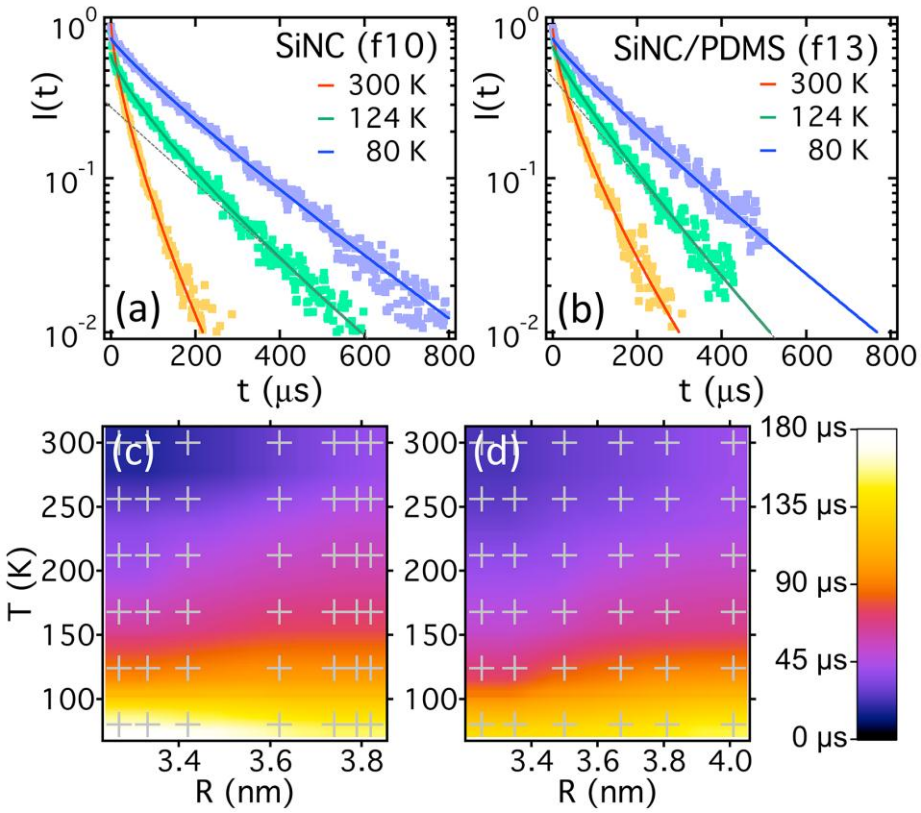

Fig. 19: (a) Temporal decay of PL for a pure QD fraction at three different temperatures and (b) an analogous plot for a PDMS nanocomposite. The curves are the stretched-exponential fits used to extract PL lifetime and the dashed lines highlight the deviation from purely exponential decay. (c) Lifetime in the plane of temperature and nanocrystal size for pure QD fractions and (d) an analogous plot for the PDMS nanocomposites, where the hatch marks indicate measurement locations.[23]

There are several implications of this data. The size dependence of the linewidth, Figure 18(c-d), is consistent with line broadening arising from electron-phonon coupling. The linewidth of both types of films increases as the temperature decreases. The slightly larger FWHM for pure QDF films suggest an environmental contribution that is reduced by the PDMS matrix. The stretching exponent increased towards 1 as the temperature decreases, reflecting a decrease in the number of available internal phonon modes. [23]

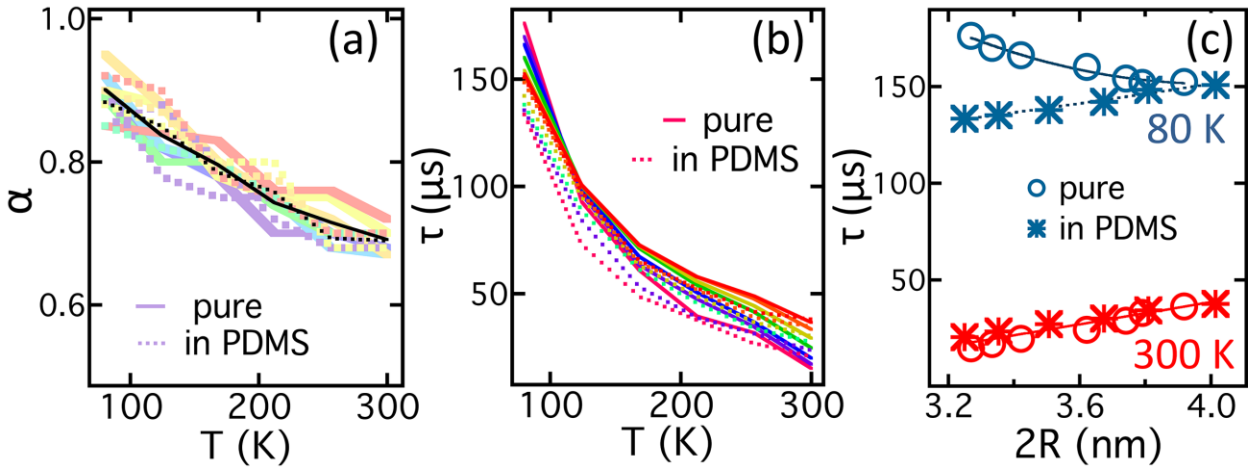

Fig. 20: (a) Stretching exponent α for all fractions as a function of temperature for both pure QD (solid) and PDMS/QD nanocomposites (dashed). The black trace is the fraction average. (b) Lifetime as a function of temperature for the pure QD fractions (solid) and PDMS nanocomposites (dashed), where the color key is the same as in Figures 1 & 2. (c) Lifetime as a function of nanocrystal size for the pure fractions and composites at 300 and 80 K. [23]

An unexpected result, however, is seen in the values of the lifetime at low temperatures. It has been shown that increased lifetimes should coincide with an increase of particle size up to the Bohr radius, or intrinsic optimal QY. [21][72] The lifetime should exhibit size dependence such that above a critical size, non-radiative events will start to dominate over QC and the lifetime will decrease. The result shown in Figure 20(b) is in striking contrast to this, as the lifetime increases with decreasing size at low temperatures for pure QDF films. This behavior might be explained through recent investigations into particle-particle interactions. It has been suggested that the efficiency of exciton transfer in many QD systems increases with decreasing QD size, [73] while it was also suggested that interactions help to enhance QY in a study of ensemble brightening. [21] These inter-particle interactions would also explain the larger increase in PL intensity upon cooling for the pure QDF films versus the PDMS/QDF films. [23]

CHAPTER 6. FIBER OPTIC TEMPERATURE PROBES USING SILICON QUANTUM DOTS

6.1. Temperature Sensing Using Quantum Dots

The temperature dependent photoluminescent properties of QDs have been recently investigated for applications as temperature probes. It was realized that to make a viable sensor, the QDs would need to be immobilized and encapsulated in some manner. This work was started in 2003 by investigating temperature dependent luminescent properties of CdSe QDs, with a ZnS shell, CdSe(ZnS), dispersed in a poly(lauryl methacrylate) (PLMA) matrix. [49]

While QD/polymer films are of great interest in constructing fiber optic temperature probes, there are several other techniques that have been explored. One early example is the production of QD doped glass as a precursor to QD doped fiber. The use of phosphate glass matrices for doping with semiconductor QDs is a way to increase the concentration of QDs as compared to silicate glasses. [50] QDs immobilized in sol-gel glasses have also been investigated as a medium for temperature sensors. [60-62] A similar idea has been applied to microstructured polymer optical fibers (mPOFs). PMMA was used to study the properties of CdSe QDs embedded as a dopant in the core of a polymer (PMMA) fiber. [51] The idea of using QDs as a fiber dopant has been explored in the field of optics, and the creation of QD based optical fiber lasers and amplifiers as an alternative for existing rare-earth doped products is a promising new area of investigation. [53] In this application a specialized type of optical fiber is used, the photonic crystal fiber (PCF). This type of fiber was first introduced to obtain lower non-linearity, lower attenuation, and unique waveguide properties. PCF is also known as “holey” fiber as it contains arrays of air holes that run along the length of the fiber core and/or cladding. [54] This allows the introduction of nanoparticles into the fiber using assorted colloidal solution methods, such as the layer-by-layer (LBL) method using polyelectrolytes, and the dip coating

method relying on capillary action. [52][55-59] The LBL method is useful for creating lengths of fiber incorporating QDs in a polymeric matrix deposited inside the length of the fiber. This is an excellent technique for applications that require a temperature reading over a relatively large area. However, the LBL method requires QDs in a polar solvent, i.e. water, whereas SiQDs require additional functionalization to become water-soluble. While there has been a significant amount of work done by several groups on the internal incorporation of QDs into fibers or glass type structures, coating the external surface of the fiber has not been significantly investigated [63], and use of SiQDs has not been previously demonstrated.

6.2. Procedure

The first objective is to coat the tip of a silica optical fiber with a film of SiQDs. The initial method used was dip coating employing a solution of QDFs/toluene. The QDFs were in solutions with a particle sizes from 3-4 nm. A 600 μm core silica multimode optical fiber, due to its large tip surface area, was used as the fiber substrate for all experiments. This particular fiber core size was the largest with simple mounting and launching equipment readily available. The coating was removed along the first several centimeters of the fiber. Initial tests indicated that the surface energy requirements for a drop of toluene to suspend from a fiber tip were not possible, and as such there was little to no QD adhesion to the fiber by dipping the fiber into the solution. Next, in an attempt to increase adhesion, the bare fiber tip was cleaned using UVO plasma, and then saturated in a 1-dodecene solution. The QDs used are passivated using this ligand, so coating the fiber tip could in theory (assuming ligand-silica wetting) increase the surface roughness of the fiber, increasing favorable interactions with the QDs. The surface energy requirements were found to still be too high in this situation. Next, tipping the vial containing the solution and allowing the solvent to completely evaporate was discovered to be an effective

method to coat the fiber tip. Special 1.3 mL v-shaped vials were eventually used to maximize the likely hood of QD adhesion to the fiber. However, even using this special type of vial, roughly half of the QDs in solution adhered to the glass vial instead of the fiber, in all attempted experiments.

Once fiber coating was observed a rough custom LED to fiber launching setup was constructed, as shown in Figure 21.

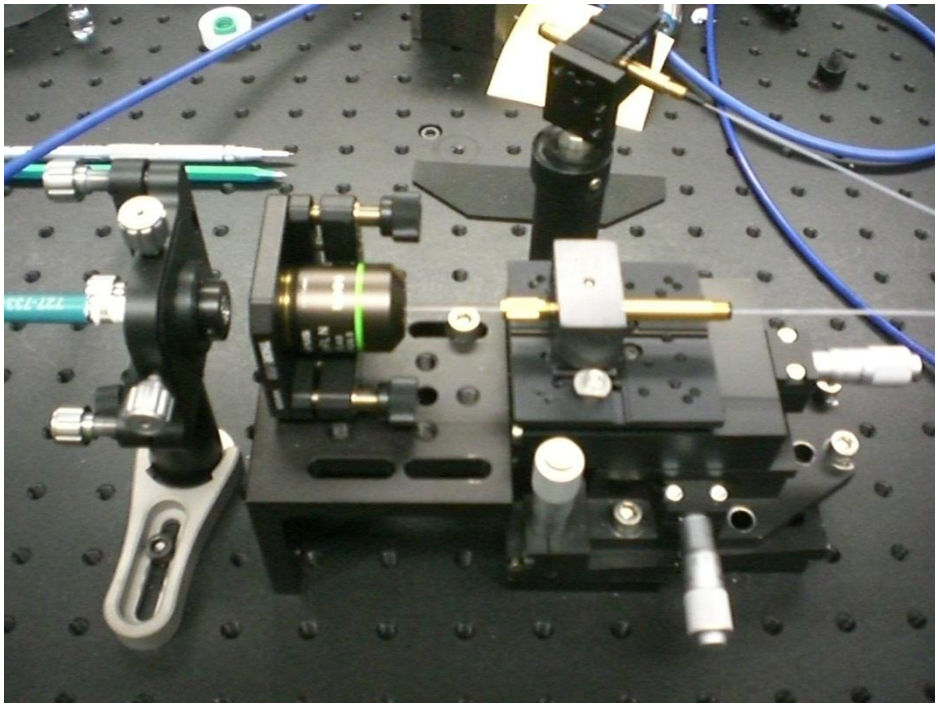

Fig. 21: LED fiber launching setup using a 20x objective.

The second step was to introduce a polymer coating, which we chose to be 20:1 PDMS. Fiber coating of PDMS/QDF was easily achieved using the procedure for coating the fibers with pure QDFs.

After the coating procedure was established, the next step was to measure PL spectra. In this setup, excitation is guided down one fiber and emission is collected from another. In order to make a small footprint sensor, the fibers must be positioned side by side. In this

configuration, scattering would be the primary pathway for PL to be excited and collected in the second fiber. The two fibers were thus stripped and adhered together. Several techniques of adhesion were investigated including epoxy, superglue, and using PDMS as glue. Finally it was discovered that careful melting of the fiber's protective polymer coating provided excellent adhesion, and ensured the fiber tips to be in contact. After some initial experimentation, it was clear that end scattering alone would not be sufficient for PL collection, and the fiber tips were thus sanded using 10 μm grit fiber sandpaper to a roughly 45^{o} angle. This angle will allow excitation light to both scatter and internally reflect into the other fiber where it can scatter and internally reflect again and propagate to the spectrometer. If both fibers are coated with QDFs, this will allow excitation on both fibers, and maximize the probability of PL photon collection. The non-treated end of the collection fiber was then butt coupled to another fiber, which was coupled to a collimating lens, through a 500 nm LP filter, and un-collimated into another fiber connected to the spectrometer. Temperature measurements were performed by removing the internal stage motion control on the Linkam cryostage and inserting the PDMS/QDF treated end.

6.3. Results and Discussion

The temperature setup used is designed to efficiently cool a liquid or flat glass slide. Due to the inherent thickness of the fiber, and the difficulty in producing sufficient stage-fiber contact to cool to 80 K, initial data collection was solely to prove the concept of a QD/PDMS treated fiber temperature probe. One fraction was used with and without a 20:1 PDMS matrix. The spectra and wavelength shifts are shown in Figure 22(b-c).

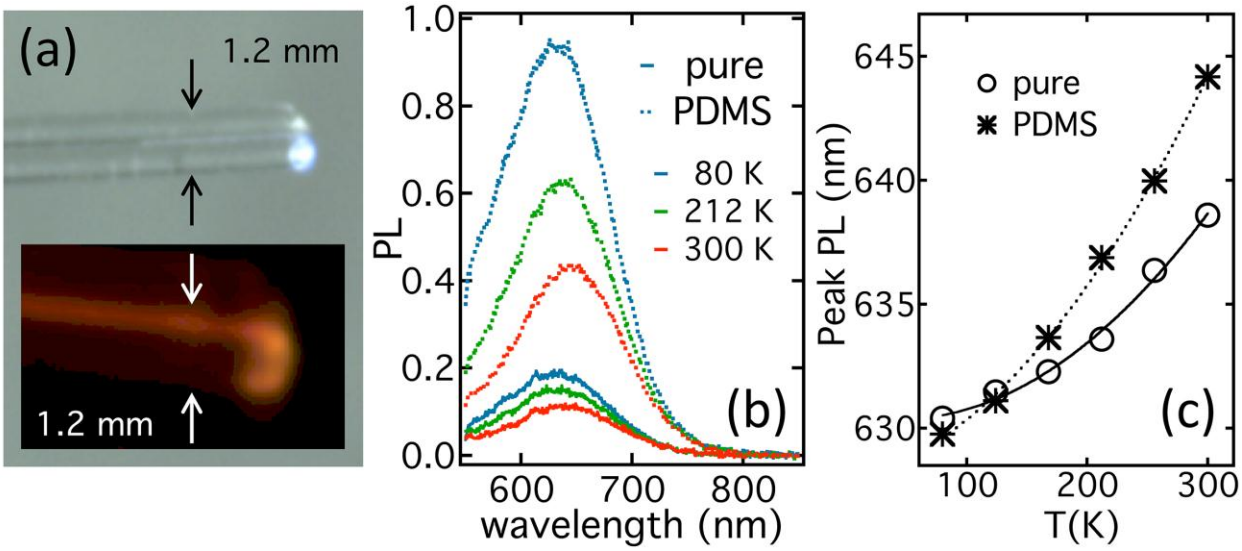

Fig. 22: (a) Normal and PL (inset) color images of a fiber-optic cryothermometer made from a middle SiNC fraction in PDMS. The excitation is introduced through the bottom fiber and PL is collected through the top. (b) Emission spectra as a function of temperature for fiber-optic devices made from both pure SiNCs and a PDMS nanocomposite. (c) Wavelength of peak PL as a function of temperature for the two devices shown in (b). [23]

As with the previous PS data, the polymer appears to increase the temperature PL sensitivity as measured by intensity wavelength. However, while it appears there is an increase in wavelength shift for the PDMS fiber, the initial recorded intensity for the PDMS fiber was approximately 5 times the pure QDF fiber. This increase of intensity coupled with the inefficiency of the fiber-stage contact area, allows few quantitative conclusions. A treated fiber is shown in Figure 22(a), where the excitation fiber exhibits a bluish glow but orange PL is clearly visible when viewed through a long-pass filter. From this image, it appears that a large portion of the PL is lost to scattering between the two fibers. A possible solution would be melting the two fibers together, however, transmission properties may then suffer. While there was not any significant data collected on this experiment, these initial findings have shown that it is possible to coat the tip of a fiber with QDs or a QD/polymer composite. This coating exhibits properties that would be expected of a comparable film.

CHAPTER 7. SUMMARY AND CONCLUSION

In conclusion, SiNCs are an interesting new material with many possible applications in optics, photovoltaics and biomedicine. One specific example of interest is in utilizing their temperature dependent properties for fiber optic cryo-temperature probes. To continue toward this goal, photoluminescent properties such as wavelength, fluorescent lifetime, FWHM, emission intensity, and photobleaching must be characterized as a function of temperature, with and without a polymer matrix, and NC size.

One important issue involved in working with SiNCs emerged during this contribution. The PL properties are extremely sensitive to environmental influences, most notably exposure to oxygen. Not only do the excited states of O_2 molecules efficiently quench the PL, but oxidation steadily blueshifts the observed PL peak wavelength over time as the optically active core becomes smaller. Oxidation was even observed for NCs in hexane solution during transportation to the laboratory, indicating that some level of oxidation may be very difficult to stop. Mitigating these two effects is of utmost importance to SiNC characterization.

First, polydisperse QD films were characterized. In the pure QD films, a basis for trends found to be pervasive throughout all experiments included a linear increase in PL with increasing excitation power, a power law correlation of $I(t)/I(0)$ observed during bleaching, and an increase in intensity with decreasing temperature. The increase in intensity during cooling can also be viewed as an increase in fluorescent lifetime, which will render each QD in an "on" state for longer intervals, thus increasing the number of radiative events. Pure QD films also displayed both an increase in wavelength and increase in stability with decreasing excitation power.

The polydisperse QDs were found to exhibit similar characteristics in various polymer matrices, i.e. PS and PMMA. QD/polymer films all showed an increase in half-life, indicating

an increase in PL stability. This effect may be a result of entropic phase separation of the polymer and NCs, causing the NCs to aggregate in the polymer matrix, which is believed to increase stability through particle-particle interactions while also shielding them from atmospheric oxygen.

While polydisperse QD characterization provides basic information about PL properties, monodisperse QDs are needed to make Si a viable material in applications. The monodisperse films were examined for both size and temperature dependent properties. The size dependency, predicted by QC, indicates a decrease in size from the Bohr radius will increase emission energy, and decrease the radiative lifetime, which were both found to be the case with one exception. In general, the temperature dependency revealed that as it cools emission energy blueshifts, FWHM increases, fluorescent lifetime increases, and the lifetime stretching exponent also increases. Inclusion of QDFs in a PDMS matrix provided identical trends as the pure QDF with one glaring exception. At low temperature, the radiative lifetime increases with decreasing size in the pure QDF films, contrary to the expected result from QC. This result may be indicative of the importance of particle-particle interactions in PL. .

Finally, coating an optical fiber with QDF/polymer nanocomposite films was found to be possible, and exhibited properties expected from observations in previous experimentation. These results show that using SiNCs as a sensing media is indeed a viable application.

REFERENCES

[1] Fujioka, K; Hiruoka, M; Sato, K; Manabe, N; Miyasaka, R; Hanada, S; Hoshino, A; Tilley, R D; Manome, Y; Hirakuri, K; Yamamoto, K, "Luminescent passiveoxidized silicon quantum dots as biological staining labels and their cytotoxicity effects at high concentration", *Nanotechnology* 2008, 19, 415102.

[2] Ding, Z; Quinn, B M; Haram, S K; Pell, L E; Korgel, B A; Bard, A J, "Electrochemistry and electrogenerated chemiluminescence from silicon nanocrystal quantum dots", *Science* **2002**, 296, 1293-1297.

[3] Warner, J H; Hoshino, A; Yamamoto, K; Tilley, R D, "Water-soluble photoluminescent silicon quantum dots", *Angewandte Chemie* **2005**, 117, 4626-4630.

[4] Park, J-H; Gu, L; Maltzahn, G; Ruoslahti, E; Bhatia, S N; Sailor, M J, "Biodegradable luminescent porous silicon nanoparticles for in vivo applications", *Nature Materials* **2009**, 8, 331-336.

[5] Liu, C-Y; Holman, Z C; Kortshagen, U R, "Hybrid solar cells from P3HT and silicon nanocrystals", *Nano Lett.* **2009**, 9, 449-452.

[6] Sychugov, I; Juhashz, R; Valenta, J; Linnros, J, "Narrow luminescence linewidth of a silicon quantum dot", *Phys. Rev. Lett*., **2005**, 94, 087405.

[7] Jurbergs, D; Rogojina, E; Mangolini, L; Kortshagen, U, "Silicon nanocrystals with ensemble quantum yields exceeding 60 %", *Appl. Phys. Lett.* **2006**, 88, 233116.

[8] Delly, B; Steigmeir, E F, "Quantum confinement in Si nanocrystals", *Phys. Rev. B.* **1992**, 47, 1391-1400.

[9] Zhou, Z; Brus, L; Freisner, R. "Electronic structure and luminescence of 1.1 and 1.4 nm silicon nanocrystals: Oxide shell versus hydrogen passivation", *Nano Lett.*, **2003**, 3, 163-167.

[10] Wolkin, M; Jorne, J; Fauchet, P; Allan, G; Delerue, C, "Electronic states and luminescence in porous silicon quantum dots: The role of oxygen", *Phys. Lett. Rev.*, **1999**, 82, 197-200.

[11] Ledoux, G; Gong, L; Huisken, F; Guillois, O; Reynaud, C, "Photoluminescence of size-separated silicon nanocrystals: Confirmation of quantum confinement", *Appl. Phys. Lett.,* **2002**, 80, 4834-4836.

[12] Onik, G M; Atkinson, D; Zemel R; Weaver, M L, "Cryosurgery of liver cancer", *Seminars in Surgical Oncology,* **2006***,* 9, 309-317.

[13] Wray, S; Cope, M; Delpy, D T: Wyatt, J S; Reynolds, E O R, "Characterization of near infrared absorption spectra of cytochrome aa3 and hemoglobin for the non-invasive monitoring of cerebral oxygention", *Biochim. Biophys. Acta.,* **1998***,* 933, 184-192.

[14] Barbagiovanni, E G; Lockwood, D J; Simpson, P J; Goncharova, L V, "Quantum confinement in Si and Ge nanostructures", *J. of Appl, Phys*., **2012**, 111, 034307.

[15] Wen, X; Van Dao, L; Hannaford, P, "Temperature dependence of photoluminescence in silicon quantum dots", *J. of Phys. D: Appl. Phys.,* **2007**, 40, 3573-3578.

[16] Mangolini, L; Thimsen, E; Kortshagen, U, "High-yield plasma synthesis of luminescent silicon nanocrystals", *Nano Lett*., **2005**, 5, 655-659.

[17] Mangolini, L; Jurbergs, D; Rogojina, E; Kortshagen, U, "Plasma synthesis and liquid phase surface passivation of brightly luminescent Si Nanocrystals", *J. of Luminescence*., **2006**, 121, 327-334.

[18] Jurbergs, D; Rogojina, E; Mangolini, L; Kortshagen, U, "Silicon Nanocrystals with ensemble quantum yields exceeding 60%", *Appl. Phys. Lett*., **2006**, 88, 233116.

[19] Sankaran, R M; Holunga, D; Flagan, R C; Glapis, K P, "Synthesis of blue luminescent Si nanoparticles using atmospheric-pressure microdischarges", *Nano. Lett*., **2005**, 5, 531.

[20] Credo, G M; Mason, M D; Buratto, S K, "External quantum efficiency of single porous silicon nanoparticles", *Appl. Phys. Lett*., **1999**, 74, 1978.

[21] Miller, J B; Van Sickle, A R; Anthony, R J; Kroll, D M; Kortshagen, U B; Hobbie, E K, "Ensemble brightening and enhanced quantum yield in size purified silicon nanocrystals", *ACS Nano,* **2012**, 6, 7389-7396.

[22] Auer, S; Frenkel, D, "Suppression of crystal nucleation in polydisperse colloids due to increase of the surface free energy", *Nature*, **2001**, 413, 711-713.

[23] Van Sickle, A R; Miller, J B; Moore, C; Anthony, R J; Kortshagen, U; Hobbie, E K, "Temperature Dependent Photoluminescence from Siloxane Nanocomposites of Size Purified Silicon Nanocrystals", *ACS Nano*, Under peer review, 12/18/2012.

[24] Hodgson, S D; Brooks, W S M; Clayton, A J; Kartopu, G; Barrioz, V; Irvine, S J C, "Enhancing blue photoresponse in CdTe photovoltaics by luminescent down-shifting using semiconductor quantum dot/PMMA films", *Nano Energy*, **2012**, 7.

[25] Li, Y; Zhang, Y; Lei, Y; Li,P; Jia, H; Hou, H; Zheng, Z, "In situ fabrication of Bi_2S_3 nanocrystal film for photovoltaic devices", *Mat. Sci. and Engineering: B*, **2012**, 177, 1764-1768.

[26] Ullah, M H; Kim, J-H; Ha, C-S, "Highly transparent *o*-PDA functionalized ZnS-polymer nanocomposite thin films with high refractive index", *Mat. Lett.,* **2008**, 62, 2249-2252.

[27] Lee, S F; Osborne, M A, "Brightening, blinking, bluing, and bleaching in a life of a quantum dot: Friend or for?", *ChemPhysChem*, **2009**, 10, 2174-2191.

[28] Deegan, R D; Bakajin, O; Dupont, T F; Huber, G; Nagel, S R; Witten, T A, "Capillary flow as the cause of ring stains from dried liquid drops", *Nature,* **1997**, 389, 827-829.

[29] Canham, L T; Keen, J M; Leong, W Y, "The structural and luminescence properties of porous silicon" UK patent application 8927709, 1989.

[30] Canham, L T, "Silicon quantum wire array fabrication by electrochemical and chemical dissolution of wafers", *Appl. Phys. Lett*., **1990**, 57, 1046.

[31] Calcott, P D J; Nash, K J; Canham, L T; Kane, M J; Brumhead, D, "Identification of radiative transitions in highly porous silicon", *J. Phys. Condens. Matter*, **1993**, 5, L91.

[32] Yoffe, A D, "Low dimensional systems: Quantum size effects and electronic properties of semiconductor microcrystallites (zero-dimensional systems) and some quasi- two dimensional systems", *Advances in Phys.,* **2002**, 51, 799-800.

[33] Barbagiovanni, E G; Goncharova, L V; Simpson, P J, "Electronic structure study of ion-implanted Si quantum dots in a SiO2 matrix: Analysis of quantum confinement theories", *Phys. Rev. B.,* **2011**, 83, 035112.

[34] Yu, P Y; Cardona, M, Fundamentals of Semiconductors: Physical and Material Properties (3^{rd} ed), Springer, Berlin, **2001**.

[35] Hybertsen, M S, "Absorption and emission of light in nanoscale silicon structures", *Phys. Rev. Lett*., **1993**, 72, 1514-1517.

[36] Delerue, C; Allan, G; Lannoo, M, "Optical band gap of Si nanoclusters", *J. of Luminescence*, **1999**, 80, 65-73.

[37] Anthony, R; Kortshagen, U, "Photoluminescence quantum yields of amorphous and crystalline silicon nanoparticles", *Phys. Rev. B.,* **2009**, 80, 115407.

[38] Ledoux, G; Gong, J; Huisken, F, "Effect of passivation and aging on the photoluminescence of silicon nanocrystals", *Appl. Phys. Lett.,* **2001**, 79, 4028-4030.

[39] Buriak, J M, "Organometallic Chemistry on Silicon and Germanium Surfaces", *Chem. Rev*., **2002**, 102, 1271.

[40] Bruhn, B; Valenta, J; Sangghaleh, F; Linnros, J, "Blinking statistics of silicon quantum dots", *Nano. Lett.,* **2011**, 11, 5574-5580.

[41] Kuno, M; Fromm, D P; Hamann, H F; Gallagher, A; Nesbitt, D J, "Nonexponential 'blinking' kinetics of single CdSe quantum dots: A universal power law behavior*", J. of Chem. Phys.*, **2000**, 112, 3117-3120.

[42] Banin, U; Bruchez, M; Alivisatos, A P; Ha, T; Weiss, S; Chemla, D S, "Evidence for a thermal contribution to emission intermittency in single CdSe/CdS core/shell nanocrystals", *J. of Chem. Phys*., **1999**, 110, 1195-1201.

[43] Cichos, F; Martin, J; Von Borczyskowski, C, "Emission intermittency in silicon nanocrystals", *Phys. Rev. B.,* **2004**, 70, 115314.

[44] Verbek, R; Van Oijen, A M; Orrit, M, "Simple model for the power-law blinking of single semiconductor Nanocrystals", *Phys. Rev. B*., **2002**, 66, 233202.

[45] Pelton, M; Grier, D G; Guyot-Sionnest, P, "Characterizing quantum-dot blinking using noise power spectra", *Appl. Phys. Lett*., **2004**, 85, 819-821.

[46] Efros, A L; Rosen, M, "Random telegraph signal in the photoluminescence intensity of a single quantum dot", *Phys. Rev. Lett.,* **1997**, 78, 1110-1113.

[47] Delerue, C; Allan, G; Lannoo, M, "Theoretical aspects of the luminescence of porous silicon", *Phys. Rev. B*., **1993**, 48, 11024-11036.

[48] Huisken, F; Ledoux, G; Guillois, O; Reynaud, C, "Light-emitting silicon Nanocrystals from laser pyrolysis", *Adv. Mater*., **2002**, 14, 1861-1865.

[49] Walker, G W; Sundar, V C; Rudzinski; Wun, A W; Bawendi, M G; Nocera, D G, "Quantum-dot optical temperature probes", *Appl. Phys. Lett*., **2003**, 83, 3555-3557.

[50] Barmenkov, Yu, O; Starodumov, A N; Lipovski, A A, "Temperature fiber sensor based on semiconductor nanocrystallite-doped phosphate glasses", *Appl. Phys. Lett*., 1998, 73, 541-543.

[51] Yu, H C Y; Leon-Saval, S G; Argyros, A; Barton, G W, "Temperature effects on emission of quantum dots embedded in polymethylmethacrylate", *Applied Optics*, **2010**, 49, 2749-2752.

[52] Larrion, B; Hernaez, M; Arregui, F J; Goicoechea, J; Bravo, J; Matias, I R, "Photonic crystal fiber temperature sensor based on quantum dot nanocoatings", *Journal of Sensors*, **2009**, 2009, 932471.

[53] Yoshie, T; Shchekin, O B; Chen, H; Deppe, D G; Scherer, A, "Quantum dot photonic lasers", *Electronics Lett*., 2002, 38, 967-968.

[54] Birks, T A; Knight, J C; Russell, P St. J, "Endlessly single-mode photonic crystal fiber", *Optics Lett.,* **1997**, 22, 961-963.

[55] Meissner, K E; Holton, C; Spillman Jr., W B, "Optical characterization of quantum dots entrained in microstructured optical fibers" *Physica E*, **2005**, 26, 377-38.

[56] Decher, G, "Fuzzy nanoassemblies: Toward layered polymeric multicomposites", *Science*, **1997**, 277, 1232-1237.

[57] Crisp, M T; Kotov, N A, "Preparation of Nanoparticle Coatings on Surfaces of Complex Geometry", *Nano Lett*., **2003**, 3, 173-177.

[58] Decher, G; Eckle, M; Schmitt, J; Struth, B, "Layer-by-layer assembled multicomposite films", *Current Opinion in Colloid & Interface Science*, **1998**, 3, 32-39.

[59] Bastida, G de; Arregui, F J; Goicoechea, J; Matias, I R, "Quantum Dots-Based Optical Fiber Temperature Sensors Fabricated by Layer-by-Layer", *IEEE Sensors Journal*, **2006**, 6, 1378-1379.

[60] Jorge, P A S; Mayeh, M; Benrashid, R; Caldas, P; Santos, J L; Farahi, F, "Quantum dots as self-referenced optical fibre temperature probes for luminescent chemical sensors" *Measurement of Science and Technology*, **2006**, 17, 1032-1038.

[61] Jorge, P A S; Maule, C; Silvia, A J; Benrashid, R; Santos, J L; Farahi, F, "Dual sensing of oxygen and temperature using quantum dots and ruthenium complex" *Analytica Chimica Acta*, **2008**, 606, 223-229.

[62] Bullen, C; Mulvaney, P; Sada, C; Ferrari, M; Chiasera, A; Martucci, A, "Incorporation of a highly luminescent semiconductor quantum dot in ZrO2–SiO2 hybrid sol–gel glass film" *J. of Mat. Chem*., **2004**, 14, 1112-1116.

[63] Yoo, J; Park, S J; Kim, J S, "Fabrication and characterization of quantum dot-based optical fiber temperature sensor", *Mol. Cryst. Liq. Cryst*., **2010**, 519, 62-68.

[64] Fagan, J A; Becker, M L; Chun, J; Nie, P; Bauer, B J; Simpson, J R; Hight Walker, A R; Hobbie, E K, "Centrifugal length separation of carbon nanotubes"*, Langmuir*, **2008***,* 24*,* 13880.

[65] Bergamini G; Alicandri-Ciufelli M; Molteni G; Villari D; Luppi MP; Genovese E, Presutti L, "Therapy of unilateral vocal fold paralysis with polydimethylsiloxane injection laryngoplasty: our experience.", *J. Voice*, **2010**, 24, 119-125.

[66] Peterson, S L; McDonald, A; Gourley, P L; Sasaki D Y, "Poly(dimethylsiloxane) thin films as biocompatible coatings for microfluidic devices: Cell culture and flow studies with glial cells." *J. Biomed. Mat. Research. Part A*, **2005**, 72A, 10-18.

[67] Olkhovets, A; Hsu, R-C; Lipovskii, A; and Wise, F W, "Size-Dependent Temperature Variation of the Energy Gap in Lead-Salt Quantum Dots." *Phys. Rev. Lett.* **1998**, 81, 3539-3542.

[68] Wang, X X; Zhang, J G; Ding, L; Cheng, B W; Ge, W K; Yu, J Z; Wang, Q M, "Origin and Evolution of Photoluminescence From Si Nanocrystals Embedded in a SiO2 Matrix." *Phys. Rev. B* **2005**, 72, 195313.

[69] O'Donnell, K P; Chen, X, "Temperature Dependence of Semiconductor Band Gaps." *Appl. Phys. Lett.* **1991**, 58, 2924-2926.

[70] Lyon, K G; Salinger, G L; Swenson, C A; White, G K, "Linear Thermal Expansion Measurements on Silicon from 6 to 340 K." *J. Appl. Phys.* **1977**, 48, 865-869.

[71] Hartel, A M; Gutsch, S; Hiller, D; Zacharias, M, "Fundamental Temperature-Dependent Properties of the Si Nanocrystal Band Gap." *Phys. Rev. B* **2012**, 85, 165306.

[72] Mastronardi, M L; Maier-Flaig, F; Faulkner, D; Henderson, E J; Kübel, C; Lemmer, U; Ozin, G A, "Size-Dependent Absolute Quantum Yields for Size-Separated Colloidally-Stable Silicon Nanocrystals." *Nano Lett.* **2012**, 12, 337-342.

[73] Lin, Z; Li, H; Franceschetti, A; Lusk, M T, "Efficient Exciton Transport between Strongly Quantum-Confined Silicon Quantum Dots." *ACS Nano* **2012**, 6, 4029-4038.

[74] Matsuyama, K; Mishima, K; Kato, T; Irie, K; Mishima, K, "Transparent polymeric hybrid film of ZnO nanoparticle quantum dots and PMMA with high luminescence and tunable emission color" *J. of Colloid and Interface Sci*., **2012**, 367, 171-177.

[75] Fernandes, R; Gracias, D H, "Self-folding polymeric containers for encapsulation and delivery of drugs", *Advanced Drug Delivery Reviews*, **2012**, 64, 1579-1589.